Remote Sensing of Environment 226 (2019) 51–73

Contents lists available at ScienceDirect

Remote Sensing of Environment

journal homepage: www.elsevier.com/locate/rse

Automatic extraction of built-up area from ZY3 multi-view satellite imagery: Analysis of 45 global cities

Chun Liu[b], Xin Huang[a,b,*], Zhe Zhu[c], Huijun Chen[a], Xinming Tang[d], Jianya Gong[a]

[a] School of Remote Sensing and Information Engineering, Wuhan University, Wuhan 430079, PR China
[b] State Key Laboratory of Information Engineering in Surveying, Mapping and Remote Sensing, Wuhan University, Wuhan 430079, PR China
[c] Department of Natural Resources & the Environment, University of Connecticut, Storrs, CT 06269, USA
[d] Land Satellite Remote Sensing Application Center, Ministry of Natural Resources of the People's Republic of China, Beijing 100048, PR China

ARTICLE INFO

Keywords:
Land cover mapping
Built-up area
High-resolution
Multi-view
ZY3

ABSTRACT

Accurate delineation of global built-up area (BUA) is fundamental to a better understanding of human development and the impacts on global environmental change. Existing global datasets of human settlement were mostly generated at medium and coarse spatial resolutions, including BUA and other impervious surfaces. With multiple high-resolution satellite constellations now available (e.g., ZiYuan-3 (ZY3), SPOT-5/6/7, Cartosat-1/2, and WorldView-2/3), identifying the global BUA explicitly from the complex landscapes becomes possible. In this study, a novel method was proposed for automated extraction of BUA at the global scale, by fusing a series of building features. Specifically, two planar features, the Morphological Building Index (MBI) and Harris corner detector, were employed to characterize the structure and corner attributes of buildings. Moreover, two multi-angular built-up indices (MABIs), i.e., Ratio Multi-angular Built-up Index (RMABI) and Normalized Difference Multi-angular Built-up Index (NDMABI), were proposed to represent the vertical properties of buildings based on multi-view images, which can further complement the planar features. 45 global cities were selected to validate the performance of the proposed method with images acquired by the ZY3 satellite constellation. The results show that the fusion of MBI and Harris corner can achieve satisfactory accuracy, i.e., 91.12%, 88.85%, 82.82% and 0.85, for the average overall accuracy (OA), user's accuracy (UA), producer's accuracy (PA), and F1-score, respectively, for all the test cities. After fusing the MABIs with the planar features, the average OA, UA, PA and F values of the final results were 92.00%, 86.20%, 89.14% and 0.87 for the RMABI, and 91.83%, 85.51%, 89.62% and 0.87 for the NDMABI, respectively. In particular, addition of the MABIs can further reduce the omission errors where medium/high rise buildings with low local contrast exist. We compared our results with two existing state-of-the-art global BUA products, Global Human Settlement Layer (GHSL) and Global Urban Footprint (GUF), which further corroborated the effectiveness of our method.

1. Introduction

Urban areas are among the most identifiable yet complex structures induced by human beings to the planet (Gamba and Herold, 2009). According to the 2017 Revision of the World Population Prospects, the world's population numbered nearly 7.6 billion as of mid-2017 and is expected to increase to 11.2 billion by the end of the 21st century (UN, 2017). Approximately 55% of the world population is living in urban areas, and the proportion keeps growing, of which almost 90% occurs in Asia and Africa (UN, 2018). The projection of global population growth and demographical urbanization indicate a massive expansion of urban land, which is mostly converted from forests, pastures, savannas, water bodies and agricultural lands, resulting in a significant impact on the regional and global ecosystem (Gamba and Herold, 2009). Accurate information on global urban area is a topic of worldwide interest with various applications, e.g., sustainable development (Gong et al., 2013; Pesaresi et al., 2013), population estimation (Yang et al., 2013), territorial monitoring (Schneider and Mertes, 2014), food security (Foley et al., 2011), crisis management (Pesaresi et al., 2015) and public health (Brockmann and Helbing, 2013; Gong et al., 2012).

Definitions of urban land differ in the existing literature, according to the problems being addressed. Most of the studies describe urban area by synthetically considering the political, demographic and socio-economic factors (UN, 2017), while others delineate urban in physical terms, i.e., the presence of artificial land covers on the earth surface (Schneider and Woodcock, 2008). Remote sensing technology has long

* Corresponding author at: School of Remote Sensing and Information Engineering, Wuhan University, Wuhan 430079, PR China.
E-mail address: xhuang@whu.edu.cn (X. Huang).

https://doi.org/10.1016/j.rse.2019.03.033
Received 3 September 2018; Received in revised form 17 March 2019; Accepted 24 March 2019
0034-4257/ © 2019 Elsevier Inc. All rights reserved.

been recognized as an effective tool to obtain the spatial extent of urban area (or human settlement, impervious surface, and built-up area) at local, regional and global scales (Deng and Wu, 2012; Schneider, 2012; Zhou et al., 2015). In this study, the physical definition of built-up area (BUA) is employed, referring to the detailed spatial delineation of the land surface which is dominantly covered by building structures (Pesaresi et al., 2016; Esch et al., 2017; Pelizari et al., 2018). BUA is the major component of impervious surface, but excluding main roads, parks and large open spaces (Qin et al., 2017).

Up to now, several global datasets related to urban area have been produced by various organizations, governments, and academia. The first-generation of global urban maps supported by Earth Observation (EO) data were mostly derived at coarse spatial resolution (300 m–10 km) (Grekousis et al., 2015; Potere et al., 2009). For example, the widely used 500 m Map of Global Urban Extent (MOD500) was generated from the Moderate Resolution Imaging Spectroradiometer (MODIS) Collection 5 coverage of the year 2001 and 2002, with a spatial resolution of ca 500 m (Schneider et al., 2009, 2010). The GlobCover (GLOBC) data derived 22 thematic land cover classes from the Medium Resolution Imaging Spectrometer (MERIS) data during the years 2005 to 2009, with 300 m resolution (Arino et al., 2007; Bontemps et al., 2011). Some researchers characterized urban areas or human activities with the Nighttime Lights (LITES) data (Zhang and Seto, 2011; Zhou et al., 2014, 2015; Xin et al., 2017), which was created from the night-time lights of the world based on the Defense Meteorological Satellite Program's Operational Linescan System (DMSP-OLS) (Elvidge et al., 2001). The annually updated project LandScan (LSCAN) represented an ambient population (average over 24 h) by integrating multiple ancillary datasets including land covers, roads, elevation, administrative boundaries, census information, medium−/high-resolution imagery, etc. (Bhaduri et al., 2002). Furthermore, the Global Impervious Surface Area Map (IMPSA) estimated the density of impervious surface by utilizing LSCAN and LITES data (Elvidge et al., 2007). The spatial resolution of the above three products was approximately 1 km. Although the first-generation products have been widely used for global analysis and applications, their problems and shortfalls are also reported, e.g., coarse resolution, limited accuracies, ambiguous definitions, low update frequencies, and inconsistencies among themselves (Chen et al., 2015; Klotz et al., 2016; Leyk et al., 2018; Pesaresi et al., 2013; Potere et al., 2009; Tatem et al., 2005).

Subsequently, the second generation of global human settlement layers with medium to high resolution (10 m–50 m) were developed in recent years, including the 30 m Global Land Cover product (GlobeLand30) (Chen et al., 2015), Global Human Settlement Layer (GHSL) (Pesaresi et al., 2015; Pesaresi et al., 2016) and Global Urban Footprint (GUF) (Esch et al., 2017; Esch et al., 2013; Esch et al., 2012). GlobeLand30 was generated with ten classes for the year 2000 and 2010, by utilizing images from Landsat satellites and the China Environmental Disaster Alleviation Satellite (HJ-1). GHSL was published by the Joint Research Centre (JRC) of the European Commission at a spatial resolution of 38 m for various epochs of BUA based on the Landsat satellite imagery of the past 40 years. Furthermore, the European Settlement Map (ESM) was also generated within the GHSL framework, representing the BUA density in Europe at 10 m resolution based on SPOT5 and SPOT6 satellite imagery (Florczyk et al., 2016). GUF was produced by the German Aerospace Center (DLR) from the TerraSAR-X and TanDEM-X radar images for the years between 2011 and 2012, at the highest spatial resolution of 12 m. A series of ancillary data (e.g., Open Street Map (OSM), MOD500, LSCAN and US National Land Cover Dataset (NLCD)) were employed for generation of the above products in training or post-editing steps.

Klotz et al. (2016) made a comprehensive cross-comparison between the high-resolution (HR) settlement layers (GUF and HR GHSL) and the low-resolution (LR) coverage (MOD500 and GLOBC) in two study sites in Central Europe, reporting an average increase from 0.31 of the LR layers to 0.58 of the HR products in terms of the Kappa coefficient. Their results demonstrated the superiority of the HR maps in terms of spatial completeness and precision, especially in low/medium density and rural/peri-urban areas. Nevertheless, considering the large diversity and complexity of settlement characteristics across the world, accuracies of the HR layers may change considerably in different areas. For example, the GUF product showed confusion between buildings and other vertical elements, such as trees and elevated roads, and the omission errors were raised when applied to sparse or low BUA with a weak vertical signal (Esch et al., 2013). Also, HR GHSL was subject to a large number of false alarms in arid regions caused by bright soil and scattered vegetation, while omitting the buildings with dark roofs (Florczyk et al., 2016; Klotz et al., 2016; Pesaresi et al., 2011). For the 38 m GHSL built-up layers (2014 collection), the commission error was about 50% by testing with the fine-scale cartography, and a relatively high confusion between BUA and other sealed surfaces (e.g., roads) was observed due to their spectral similarity (Pesaresi et al., 2016). Leyk et al. (2018) validated the accuracy of GHSL across rural-urban trajectories in the United States, reporting high accuracy in urban areas but relatively low accuracy in rural regions.

Besides the existing global products, a series of state-of-the-art urban mapping methodologies have been proposed and applied over local regions, such as in the Twin Cities (Minnesota) Metropolitan Area (Yuan et al., 2005), Washington, D.C.-Baltimore, MD megalopolis (Sexton et al., 2013; Song et al., 2016), Beijing (Li et al., 2015a), Wuhan (Hu et al., 2018), Pearl River Delta (Zhang and Weng, 2016) and China (Huang et al., 2018b). In particular, Zhu et al. (2012) and Qin et al. (2017) integrated Landsat and Advanced Land Observation Satellite (ALOS) Phased Array type L-band Synthetic Aperture Radar (PALSAR) data for land cover classification and BUA extraction, respectively, showing the benefits of the fusion of optical and radar data for mapping BUA.

In recent decades, many HR satellites (e.g., QuickBird, SPOT, WorldView, Planet Labs, GaoFen series, SuperView) have been launched. High spatial resolution images can reduce the mixed-pixel phenomenon and contain rich textural information, therefore have the potential to distinguish BUA from other surface features explicitly (e.g., roads, bridges, open spaces, parks, and soil). However, the intrinsic heterogeneity of BUA, including building materials (e.g., concrete, bitumen, stone, clay, metal), construction styles (e.g., color, size, height), and urban functions (e.g., residential, commercial, industrial, educational), increases the difficulty of their accurate detection from HR imagery. Also, BUA exhibit similar characteristics to other ground objects (e.g., soil, rocks, paved road, squares), which leads to confusion when only spectral features are considered. Due to the massive data volume, timely and adequate selection of training samples is challenging for supervised methods. Although several unsupervised built-up indicators exist, such as PANTEX (Pesaresi et al., 2008), local feature points (Sirmacek and Unsalan, 2010), Harris corners (Kovács and Szirányi, 2013; Tao et al., 2013) and morphological building index (MBI) (Huang and Zhang, 2011), their stability and robustness over global areas still need more investigation.

Through cross-track or along-track imaging mode, a number of HR satellites (e.g., ZiYuan-3 (ZY3), SPOT-5/6/7, Cartosat-1/2, and WorldView-2/3) have the ability of collecting multi-view images. Multi-view images allow the retrieval of three-dimensional information, which have proven useful for the interpretation of urban scenes with complex building environments (Taubenböck et al., 2013). The digital surface model (DSM) was the most widely applied method to derive height information for urban classification, building extraction, change detection (Huang et al., 2017a; Longbotham et al., 2012; Qin and Fang, 2014), etc. However, the generation of DSM at a large scale is time consuming and has a high computation cost. Moreover, the quality of the satellite-derived DSM can be largely affected by image matching errors, effects of incomplete and blurred boundaries, especially in urban areas due to the occlusion and large disparity of buildings (Aguilar et al., 2014). Longbotham et al. (2012) investigated the potentialities of

WorldView-2 multi-angle image sequences for urban classification in Atlanta, by considering the spatial and spectral information from the multi-view images. The authors found that the employment of multi-angle images can better differentiate some classes that were not well identified by a single-view image (e.g., skyscrapers and bridges). On the other hand, the spectral distortions in multi-view images caused by angular effects were analyzed in Matasci et al. (2015), based on two WorldView-2 in-track sequences. Their results indicated that pre-processing of the multi-view images by histogram matching or atmospheric compensation can remarkably enhance the portability of the classification models across the sequences. More recently, Huang et al. (2018a) proposed angular difference features (ADFs) for urban scene classification from ZY-3 multi-view images. Specifically, ADFs were constructed at pixel, feature and label levels, respectively. Experiments in Shenzhen and Beijing test images show that the ADFs can effectively complement the spectral bands to improve classification accuracy, especially for some man-made classes with similar spectral characteristic (e.g., roads and buildings). The studies aforementioned confirmed the potential of multi-view images for urban mapping. However, they focused on urban classification by supervised machine learning techniques with the collection of training samples. In addition, their generalization ability over global areas has not been verified due to their limited and small test images. To the knowledge of the authors, no automatic multi-angular indices for large area BUA extraction exist in the current literature.

In this research, a novel planar-vertical feature fusion method for BUA extraction from ZY3 multi-view imagery was proposed. Aiming at establishing a robust framework for global BUA extraction, a set of planar and vertical features were constructed and combined, by considering their different capabilities of delineating various building characteristics. Specifically, the features employed in this study included:

1) Planar: including the recently developed Morphological Building Index (MBI) and the Harris corner detector. MBI was able to depict the detailed structure of individual buildings, and the Harris corner detector can highlight the corners of buildings.
2) Stereoscopic: when multi-view images were available, a series of multi-angular built-up indices (MABIs), including the Ratio Multi-angular Built-up Index (RMABI) and Normalized Difference Multi-angular Built-up Index (NDMABI), were proposed to further describe the stereo property of BUA and complement the planar features.

The workflow was free from training sample collection and needed little manual intervention. We verified the generality and stability of the proposed method for mapping BUA in various cities around the world based on ZY3 HR multi-view images. A large number of images were applied, involving 45 cities in 21 countries worldwide and covering a total area of 51,776 km^2. The remainder of this work was organized as follows. The subsequent section describes the study areas and data. Section 3 presents the proposed methodology and workflow. Section 4 depicts the experiment and results. We compared our results with Global Human Settlement Layer (GHSL) and Global Urban Footprint (GUF) in Section 5, followed by the discussions about the effects of the multi-features and post-processing. The conclusions are drawn in Section 6.

2. Study areas and data

A total of 45 cities located in the six continents were selected as test areas (Fig. 1). The study areas span wide longitude and latitude, and represent a variety of urban landscapes, including coastal (e.g., Los Angeles, Algiers, Cape Town), inland (e.g., Moscow, Delhi), mountainous (e.g., Santiago, Lhasa, Addis Ababa), flat (e.g., Wuhan, Changsha, Shanghai), and desert areas (e.g., Riyadh). They range from megacities (e.g., Beijing, Tokyo, Washington), medium-sized cities (e.g., Hefei, Baghdad), to small towns (e.g., Chakwal, Heidelberg). Both developed and developing cities are considered. In particular, more developing cities in China are selected, since these areas are undergoing rapid urbanization processes with more heterogeneous and tumultuous landscapes.

The high quality ZY3 images (cloud coverage < 10%), provided by the Land Satellite Remote Sensing Application Center (LASAC), Ministry of Natural Resources of the People's Republic of China, were employed for all the test cities. The ZY3 stereo mapping satellite constellation is composed of two satellites, i.e., ZY3-01 and ZY3-02, which were launched on 9th January 2012, and 30 May 2016, respectively (Tang et al., 2013, 2015). Phased 180° apart in the same orbit, the deployment of the two satellites can significantly increase the efficiency and capability of data acquisition. The ZY3 01 and 02 satellites were designed with similar specifications. The payloads of each ZY3 satellite include panchromatic three-line array cameras (TLC) and a multispectral (MS) camera. The TLC is composed of a nadir (NAD) camera as well as two oblique cameras viewing in the forward (FWD) and backward (BWD) modes with fixed inclinations of ± 22°. The spatial resolution of the two oblique cameras of ZY3-02 is enhanced from 3.5 m (ZY3-01) to 2.5 m. The planar and vertical geometric accuracies of ZY3-01 were reported as 10 m and 5 m without ground control points (GCPs), but better than 3 m and 2 m with a few GCPs, respectively (Wang et al., 2014; Tang et al., 2015). More detailed specifications for

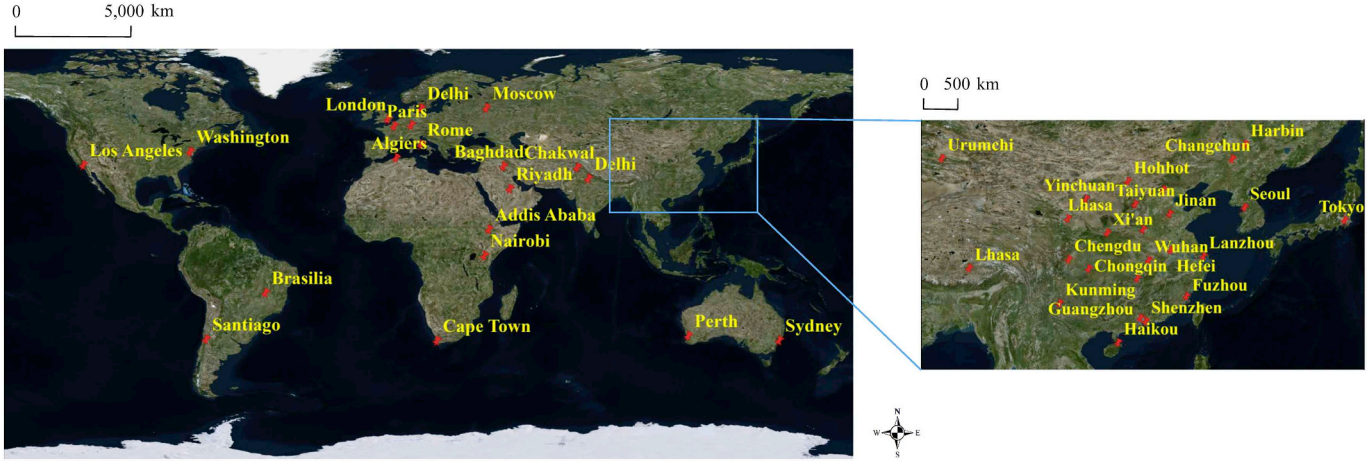

Fig. 1. Global distribution of the test cities (base map credit: Bing Maps).

Table 1
Specifications for ZY3 01 and 02 satellites (PAN = panchromatic bands, MS = multispectral bands, FWD = forward, BWD = backward, and NAD = nadir).

	ZY3-01	ZY3-02
Launch time	January 9, 2012	May 30, 2016
Orbit altitude	506 km	505 km
Type	10:30 a.m. Sun-synchronous	10:30 a.m. Sun-synchronous
Revisit cycle	5 days	5 days
Swath width	> 50 km	> 50 km
Spatial resolution	PAN-NAD: 2.1 m	PAN-NAD: 2.1 m
	PAN-FWD: 3.5 m	PAN-FWD: 2.5 m
	PAN-BWD: 3.5 m	PAN-BWD: 2.5 m
	MS: 5.8 m	MS: 5.8 m
Wavelength	PAN: 500–800 nm	PAN: 500–800 nm
	Blue: 450–520 nm	Blue: 450–520 nm
	Green: 520–590 nm	Green: 520–590 nm
	Red: 630–690 nm	Red: 630–690 nm
	Infrared: 770–890 nm	Infrared: 770–890 nm

the ZY3 satellite constellation are presented in Table 1. The notable advantages of ZY3 lie in the following aspects: 1) availability of nadir images makes it convenient to delineate the accurate footprints of BUA; 2) benefiting from the standard along-track system, HR three-viewing images of the same scene can be acquired nearly simultaneously (within half a minute) (Tong et al., 2015); and 3) multi-spectral, planar and vertical information can be exploited. These virtues of the ZY3 images make them very suitable for BUA extraction. Table 2 lists the data used in this study, where 38 images were acquired by ZY3-01 and 7 images by ZY3-02. The last column of Table 2 indicates the number of the available viewing angles. For example, 3 means NAD, FWD and BWD images were available, while 1 indicate only nadir image was available. For most of the cities, multi-view images were available, except for Haikou, Nairobi, London, Rome, and Sydney.

3. Methodology

The proposed feature extraction and fusion method for detecting BUA were based on their spectral, morphological, corner response, and stereo characteristics. The morphological building index (MBI), and the Harris corner operator were used to represent the planar features of buildings (Huang and Zhang, 2011, 2012; Tao et al., 2013). Also, by courtesy of the ZY3 multi-view observation mode, the vertical feature MABI was developed, to reflect the stereo property of BUA. MABI was able to further complement the two planar features, especially in dark building areas which were usually omitted by planar features due to their low luminance and small local contrast. MBI, Harris corner, and MABI features can characterize building attributes from different aspects, and complement each other. To reduce commission errors, a series of post-processing steps were also conducted by imposing the spectral and shape information as constraints. By fusion of the above features, an intensity map of the BUA was produced, and the final result was obtained with a fine-tuned threshold. The processing chain of the proposed method is illustrated in Fig. 2.

3.1. Pre-processing

The pre-processing steps included image calibration to top-of-the-atmosphere (TOA) reflectance, ortho-rectification, registration, and pan-sharpening. The multi-spectral bands and panchromatic FWD, BWD of ZY3 images were all registered to the NAD image by applying polynomial warping with the automatically generated tie points. The registration error was less than one pixel. The MS and NAD images were fused by the Gram Schmidt transformation (Chavez et al., 1991). To compensate for the angular divergence, a relative normalization was performed between the multi-view panchromatic images by a histogram matching method (Matasci et al., 2015). Note that all images were resampled to a uniform spatial resolution of 2.5 m. The pan-sharpened image was prepared for the generation of MBI and Harris corner features. Meanwhile, the multi-view NAD, FWD and BWD images were used for the calculation of MABI features.

3.2. Feature extraction

3.2.1. Morphological building index (MBI)

The brightness image, defined as the maximum TOA reflectance value of each pixel from the visible bands, is regarded as suitable for building detection (Pesaresi et al., 2011), and hence, used as the input image for the subsequent MBI and Harris feature extraction.

The morphological building index (MBI) (Huang and Zhang, 2011, 2012) is an automatic building detector, aiming at describing the spectral-spatial characteristics of buildings (e.g., size, local contrast,

Table 2
The ZY3 images used in this study.

City	Satellite sensor	Acquisition date	Area (km^2)	Angle number	City	Satellite sensor	Acquisition date	Area (km^2)	Angle number
Beijing	ZY3-01	20170515	1591.10	3	Tokyo	ZY3-01	20140331	1189.79	3
Harbin	ZY3-02	20170529	1319.00	3	Seoul	ZY3-01	20131027	1537.05	3
Changchun	ZY3-01	20170615	1280.70	3	Delhi	ZY3-01	20141204	537.37	3
Hohhot	ZY3-01	20140726	532.63	3	Chakwal	ZY3-01	20170402	679.66	3
Taiyuan	ZY3-01	20150423	583.58	3	Riyadh	ZY3-02	20170424	1385.99	3
Yinchuan	ZY3-01	20170706	961.23	3	Baghdad	ZY3-02	20160702	1499.58	3
Lanzhou	ZY3-01	20170809	191.73	3	Addis Ababa	ZY3-01	20131203	477.77	3
Xi'an	ZY3-01	20150512	575.14	3	Nairobi	ZY3-01	20150130	1646.36	1
Zhengzhou	ZY3-02	20160604	547.35	3	Algiers	ZY3-01	20160329	1136.80	3
Jinan	ZY3-01	20170530	1154.30	3	Cape Town	ZY3-01	20140907	1811.53	3
Hefei	ZY3-01	20160828	1619.70	3	Washington	ZY3-01	20120630	1338.21	3
Shanghai	ZY3-01	20141015	1258.40	3	Los Angeles	ZY3-01	20130129	1202.13	2
Wuhan	ZY3-01	20130812	799.12	3	Santiago	ZY3-01	20121203	1766.62	3
Changsha	ZY3-02	20170213	1162.70	3	Brasilia	ZY3-01	20140715	1362.93	3
Fuzhou	ZY3-01	20170926	1339.00	3	Heidelberg	ZY3-01	20120918	883.76	3
Guangzhou	ZY3-01	20150414	1086.00	3	London	ZY3-01	20130708	1505.49	1
Shenzhen	ZY3-01	20131223	1793.70	3	Moscow	ZY3-01	20140531	1284.76	3
Haikou	ZY3-01	20160506	1739.20	1	Rome	ZY3-01	20140720	1162.88	1
Kunming	ZY3-01	20160117	820.29	3	Copenhagen	ZY3-01	20130927	1553.30	3
Chengdu	ZY3-01	20170508	910.91	3	Paris	ZY3-02	20170626	1187.47	3
Chongqing	ZY3-01	20170607	1453.80	3	Sydney	ZY3-01	20121125	1652.96	1
Lhasa	ZY3-01	20140603	402.39	3	Perth	ZY3-01	20120618	898.64	3
Urumchi	ZY3-02	20160603	952.77	3					

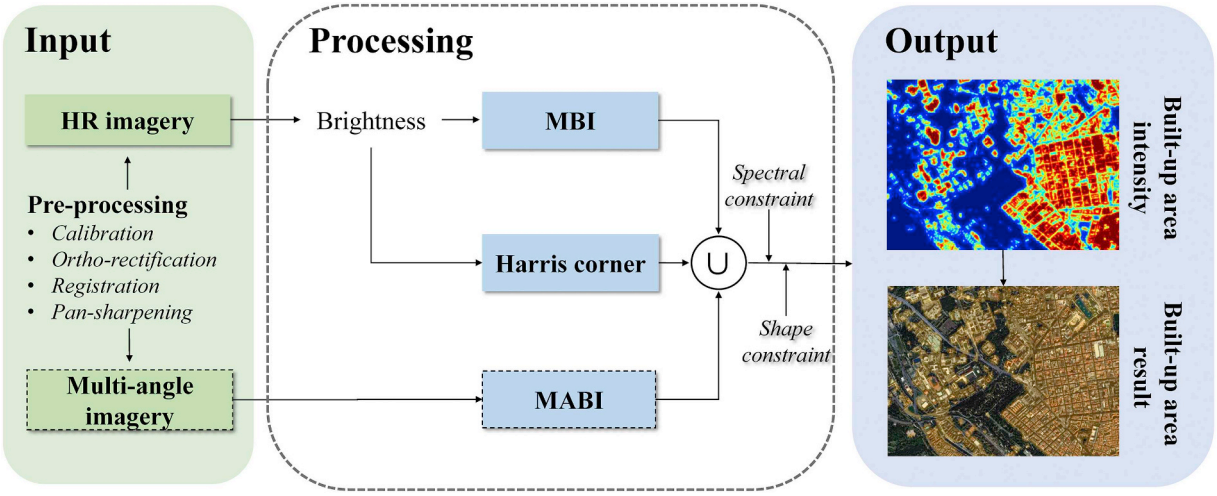

Fig. 2. Processing chain for BUA extraction in this paper. The multi-angle images are used when available.

brightness, and isotropy) with a set of morphological operators. It is constructed by considering the spectral-spatial characteristics of the relatively high reflectance of roofs as well as their spatially adjacent shadows that can lead to high local contrast. Specifically, the differential morphological profiles (DMPs) (Pesaresi and Benediktsson, 2001) of the multi-scale and multi-directional morphological white top-hat by reconstruction (WTH) transform are used to highlight buildings:

$$\mathrm{MBI} = \frac{\sum_{s\in S}\sum_{d\in D}(\mathrm{DMP} - \mathrm{WTH}(s,d))}{N_s \times N_D} \tag{1}$$

where the WTH operator is defined as:

$$\mathrm{WTH}(s,d) = B - \gamma_B^{re}(s,d) \tag{2}$$

where B indicates the brightness image, and $\gamma_B{}^{re}$ is the opening-by-reconstruction of the brightness image based on a set of linear structural elements (SE), s and d represent the size/scale and direction of the SE, and N_s, N_D denotes the total number of scales and directions, respectively. $s(s_{min}, s_{max}, N_s)$ should be adjusted according to the building size and image resolution (2.5 m in this study). Normally, the dimension of buildings is in the range of 10–350 m, including small houses and large commercial/industrial structures. Therefore, the values of s_{min}, s_{max} *and* N_s were set to 4, 140 and 4, respectively, in our experiments. Four directions were set (N_D = 4) at 0°, 45°, 90°, and 135°. A high MBI value signifies that this structure is likely to be a building.

Since shadows can be considered as evidence for verification of buildings on HR imagery (Ngo et al., 2017; Ok, 2013), they serve as a contextual constraint to remove false alarms of MBI (e.g., bright soil, squares, roads). The shadow mask was generated by segmenting the near-infrared band of the imagery with the threshold determined by a histogram thresholding approach (Dare, 2005; Song et al., 2014). Subsequently, the shadows were dilated with three pixel's distance towards their corresponding buildings which were in the opposite direction to the solar illumination angle with a linear SE (Huang et al., 2017b). By considering the spatially adjacent relationship between a building and its shadow, the candidate building is retained when there is an overlap between the dilation area and the building object; otherwise, it is removed.

3.2.2. Harris corner detector

The Harris corner detector (Harris and Stephens, 1988) is a widely used technique for extraction of salient points. With the capability of highlighting the corners of buildings, the Harris corner response has been found to be closely related to the existence of BUA (Hu et al., 2016; Tao et al., 2013; Gueguen and Pesaresi, 2011). Based on the local auto-correlation function, the local variation can be measured by shifting a small window around the target pixel, and the pixel is considered as a corner point when it shows a significant change in all directions. The Harris corner response function is given by:

$$H(M) = det(M) - k\ tr^2(M) \tag{3}$$

where *det(M)* and *tr(M)* are the determinant and trace of the matrix *M*. The value of *k* can be empirically determined in the range [0.04, 0.15] (Gueguen and Pesaresi, 2011), and in this study *k* was set to 0.06. The matrix M is composed of four elements computed from the image gradients:

$$M = G(x,y)\otimes\begin{bmatrix} B_x^2 & B_xB_y \\ B_xB_y & B_y^2 \end{bmatrix} \mathrm{M} = \begin{bmatrix} \mathrm{I_x^2 I_x I_y} \\ \mathrm{I_x I_y I_y^2} \end{bmatrix} \tag{4}$$

where B_x and B_y *are* the derivatives of the brightness images in the horizontal and vertical direction. $G(x,y)$ is the Gaussian function and $\otimes$ is the convolution operator.

3.2.3. Multi-angular built-up index (MABI)

In multi-view images, vertical structures exhibit angular variations due to their height, i.e., different spectral and structural features in different viewing angles, while low-lying objects have more consistent characteristics. Based on this phenomenon, in this research, the Multi-angular Built-up Index (MABI) was proposed to describe the angular difference of buildings. By courtesy of the three-line-array mode of ZY3 satellites, NAD, FWD and BWD panchromatic images of the same scene can be collected quasi-simultaneously. This unique characteristic allows us to highlight the variation caused by the viewing angle, since other factors such as solar illumination and atmospheric condition can be regarded consistent among the multi-view images. We proposed two approaches to calculate MABI: 1) Ratio Multi-angular Built-up Index (RMABI) (Eq. (5)), and 2) Normalized Difference multi-angular built-up index (NDMABI) (Eq. (6)).

$$\mathrm{RMABI} = \max\left\{\frac{X_n}{X_f}, \frac{X_n}{X_b}, \frac{X_f}{X_b}, \frac{X_f}{X_n}, \frac{X_b}{X_n}, \frac{X_b}{X_f}\right\} \tag{5}$$

$$\mathrm{NDMABI} = \max\left\{\frac{|X_n - X_f|}{\max(X_n, X_f)}, \frac{|X_n - X_b|}{\max(X_n, X_b)}, \frac{|X_f - X_b|}{\max(X_f, X_b)}\right\} \tag{6}$$

where X_f, X_n and X_b is the reflectance of FWD, NAD and BWD images, respectively. RMABI calculates the maximum value of the ratios between the stereo image pairs, and NDMABI is the maximum value of the differences normalized by their reflectance values. RMABI and NDMABI can highlight the angular variations of the off-terrain objects, but suppress the low-lying objects (e.g., roads, grass, water, soil) at the

same time. These indices aim to maximize the contrast between vertical structures and the ground surface, and therefore are able to detect buildings from multi-view images.

3.3. Feature fusion and post-processing

The MBI, Harris corner and MABIs had different capabilities to delineate various building characteristics. However, they were subject to some commission and omission errors. Specifically, MBI delineated buildings with different size and shape, but false alarms might appear in the cases where the objects had similar spectral and spatial characteristics to buildings. The omission of MBI was related to the dark roofs due to their low brightness and contrast with the surroundings. The Harris detector highlighted building corners, but it was also sensitive to texture areas such as trees and cropland in HR imagery, and hence leaded to false alarms in these regions. On the other hand, large buildings, like industrial and commercial architecture, might be omitted by Harris detector due to their sparse corner points. MABI was capable of suppressing ground objects. However, false alarms could be induced by other vertical structures (e.g., trees, viaduct, and mountain ridge), and omission errors occurred for low rise buildings, due to the insignificant angular variation.

To minimize the omission errors, the aforementioned multiple features were merged to make full use of their complementary information, and subsequently, a series of post-processing steps were conducted to reduce the commission errors.

1) *Feature fusion:* as mentioned previously, the two planar features (i.e., MBI and Harris corner) and the vertical MABI were separately binarized and then merged by using a union operation, in order to reduce omission errors.
2) *Post-processing*: including the spectral and shape constraints, to suppress the false alarms caused by the feature fusion. The spectral constraint was implemented by taking advantages of the vegetation and water indices to remove most of the commission errors induced by grass, trees, cropland and water areas. The soil-adjusted vegetation index (SAVI) (Huete, 1988) was chosen due to its better performance than the normalized differential vegetation index (NDVI) in the areas where plant cover was generally low (Sun et al., 2016). The normalized difference water index (NDWI) (McFeeters, 1996) was used to filter out the false alarms induced by bright water areas. With respect to the shape constraint, the minimum area and length-width ratio of the detected objects were considered, to remove the small and narrow objects (e.g., noise and roads).

3.4. Generation of built-up area

A multi-scale strategy was adopted to produce the BUA intensity (BUAI) map considering the multi-scale characteristics of BUA (Li et al., 2015b). Specifically, the BUAI was computed by averaging the building densities derived from a set of grids of different size. In particular, the building density in each grid was generated by sliding a set of half-overlapped grids to reduce the blurred boundaries caused by the moving windows. Finally, the BUA result was obtained by thresholding the BUAI feature map.

In Fig. 3, three examples are utilized to demonstrate the feature extraction (MBI, Harris corner and RMABI) (Fig.3(b~d)), building map generated by feature fusion [Fig. 3(e)], BUAI [Fig. 3(f)], and the final results [Fig. 3(g)]. Patch #1, which is an urban scene, shows both congregated and detached buildings. Patch #2 exhibits villages with small houses in a rural area, and patch #3 is a typical residential area with dense and high buildings. In general, the capabilities of the three features are different but complementary in delineating different building characteristics. From Fig. 3(b), it can be seen that the MBI can effectively delineate buildings with different size and shape, showing its potential for generating accurate BUA boundaries. Fig. 3(c) indicates that the Harris detector has a high response to corners of buildings, and it is therefore particularly useful to highlight small buildings (patch #2). In Fig. 3(d), the RMABI is efficacious for detecting medium and high-rise buildings, including the buildings with low reflectance in the imagery (e.g., patch #3). The fused building map is displayed in Fig. 3(e), showing that most of the BUA can be extracted after a combination of the three features. The BUAI features in Fig. 3(f) depict the intensity of BUA, and finally, Fig. 3(g) illustrates the final results.

3.5. Accuracy assessment

To quantitatively validate the results of the proposed method, we manually interpreted 1000 samples (simple random) based on the nadir pan-sharpened ZY3 imagery for each test site. The high-resolution aerial and satellite photo archives on their closest dates in Google Earth™ were used to assist the interpretation when there was confusion for identifying the land cover types. In total, the validation data consist of 17,246 BUA pixels and 27,754 non-BUA pixels, respectively. The confusion metrics were then calculated from the sample set for accuracy assessment. The area based statistical inference (Foody, 2002; Stehman, 2013; Olofsson et al., 2014) was conducted to estimate the accuracy scores including overall accuracy (OA), producer's accuracy (PA), user's accuracy (UA), and F1-score (F), where PA and UA address the completeness and precision of the detection, respectively, and F measures the trade-off between PA and UA.

4. Experiment and results

4.1. Parameter setting

A set of thresholds were required in the proposed method for feature binarization. We defined $\theta_1 \sim \theta_4$ as the binary thresholds for MBI, Harris, MABI, and BUAI, respectively. Note that the MBI, MABI and BUAI were normalized to the range [0, 1]. According to our previous experiments (Huang et al., 2017b; Huang and Zhang, 2011, 2012), θ_1 was fixed to a small value of 0.1 in this study, so that more building candidates could be retained before the post-processing steps. θ_2 was set to a very small value (0.01) to extract most of the corner points, as the values of non-corner areas in the Harris corner feature were negative or close to 0. The MABI threshold θ_3 was suggested in the range [0.8, 0.9] based on fine-tuning. In our experiments, its value was fixed to 0.9 for both RMABI and NDMABI, in order to suppress false alarms from the low-lying objects. θ_4 was defined as the threshold to obtain the final result from the BUAI. Its value was set to 0.1 in this study, by tuning in a series of representative cities.

4.2. Results

The final results of five representative cities are presented in Fig. A1, the GHSL built-up layer and MOD500 product are also shown for comparison. Generally, the three products have similar spatial distribution patterns of BUA, but our results demonstrate the most accurate representation of BUA with the finest spatial details. Specifically, our results can not only show more details within the urban cores, but also detect the small villages in the rural areas, attributed to the higher resolution images used. For instance, in the urban areas of Riyadh and Perth, our results can distinguish BUA from non-BUA areas such as parks, rivers, main roads and bare land. Meanwhile, in the rural areas of Xi'an, Changsha, and Algiers, small villages and isolated houses that may be omitted by GHSL and MOD500, can be detected by our method.

To show more details of our results, zoom-in regions in several cities are illustrated in Fig. 4, with the original images and results superimposed on the images. These subsets were clipped from the urban core, peri-urban and rural areas, respectively, representing different scenes in the study images. In downtown areas, such as the subsets in Beijing, Copenhagen, Paris, and Los Angeles, small residential areas and

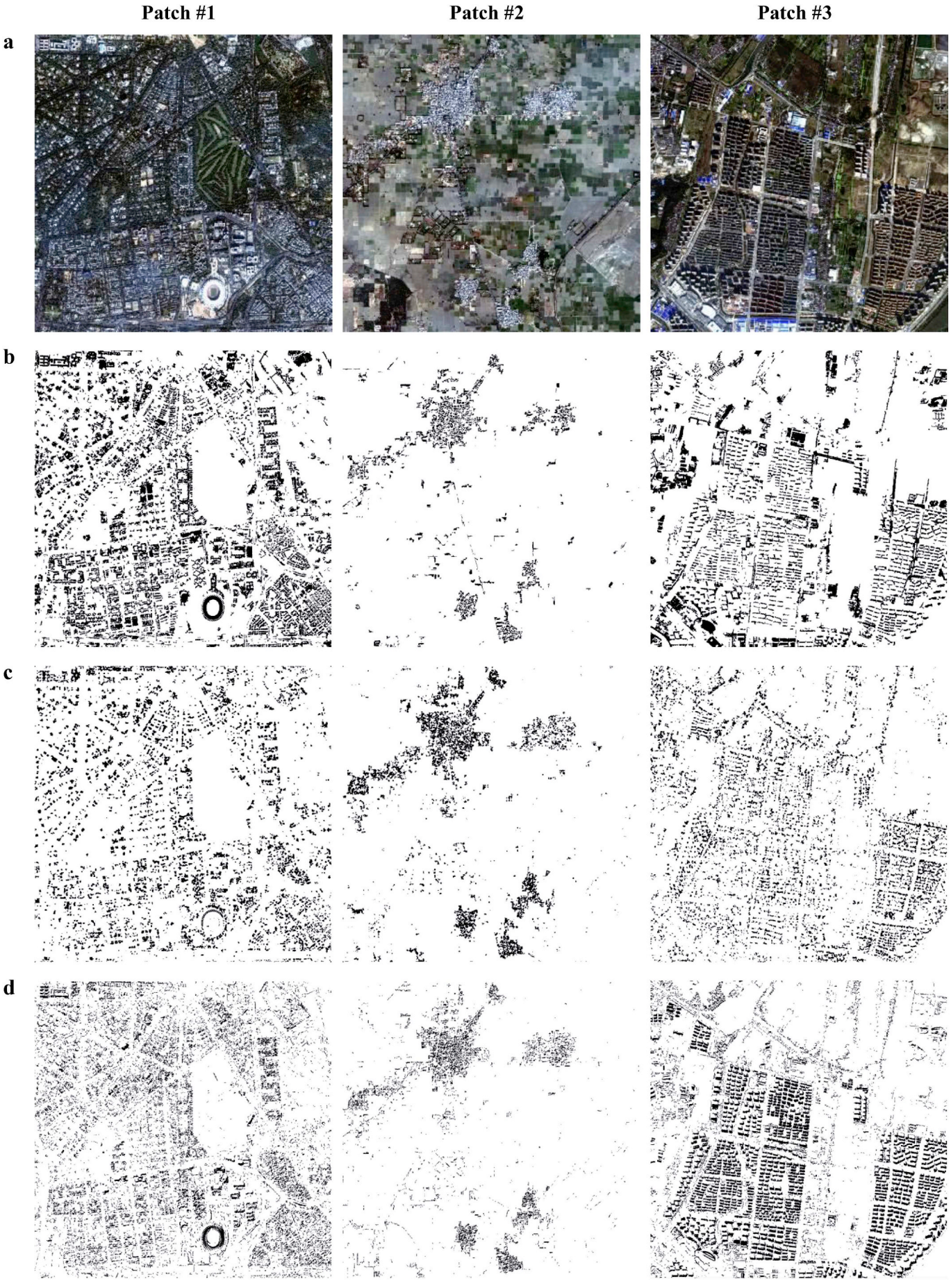

(caption on next page)

Fig. 3. Demonstration of the features and results of the proposed method in three representative patches: (a) the true color images of the three patches; (b~d) MBI, Harris corner and RMABI features, respectively; (e) fused building maps; (f) BUAI features; (g) the final results overlaid with satellite images.

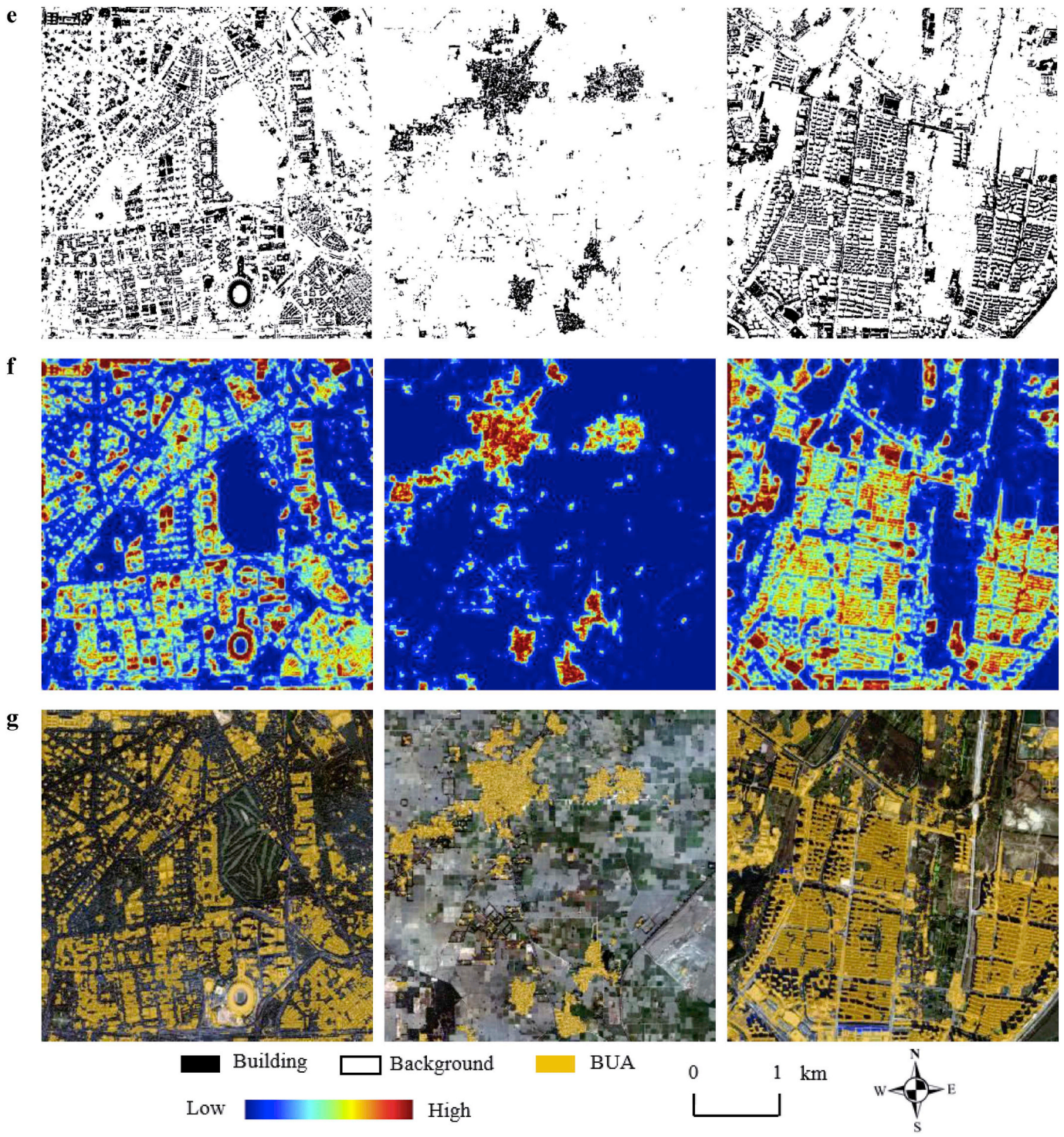

Fig. 3. (*continued*)

large commercial areas were extracted, while the main roads, rivers or parks were removed. In peri-urban areas, e.g., the subsets in Algiers, London and Cape Town, the vegetated areas or large bare soil/ground were suppressed. In rural areas, e.g., the subsets in Xi'an, small villages can be accurately detected, and at the same time, the cropland and soil were excluded. Other ground objects, such as the airport runway in the Cape Town subset, and the salt lake in Perth subset were effectively filtered out by our method.

The quantitative accuracy scores of each city are listed in Table A1. Please notice that the multi-view images were available in 40 cities (not available in the remaining 5 cities), therefore, the results could be generated by using both the planar features (written as PLA) and all the

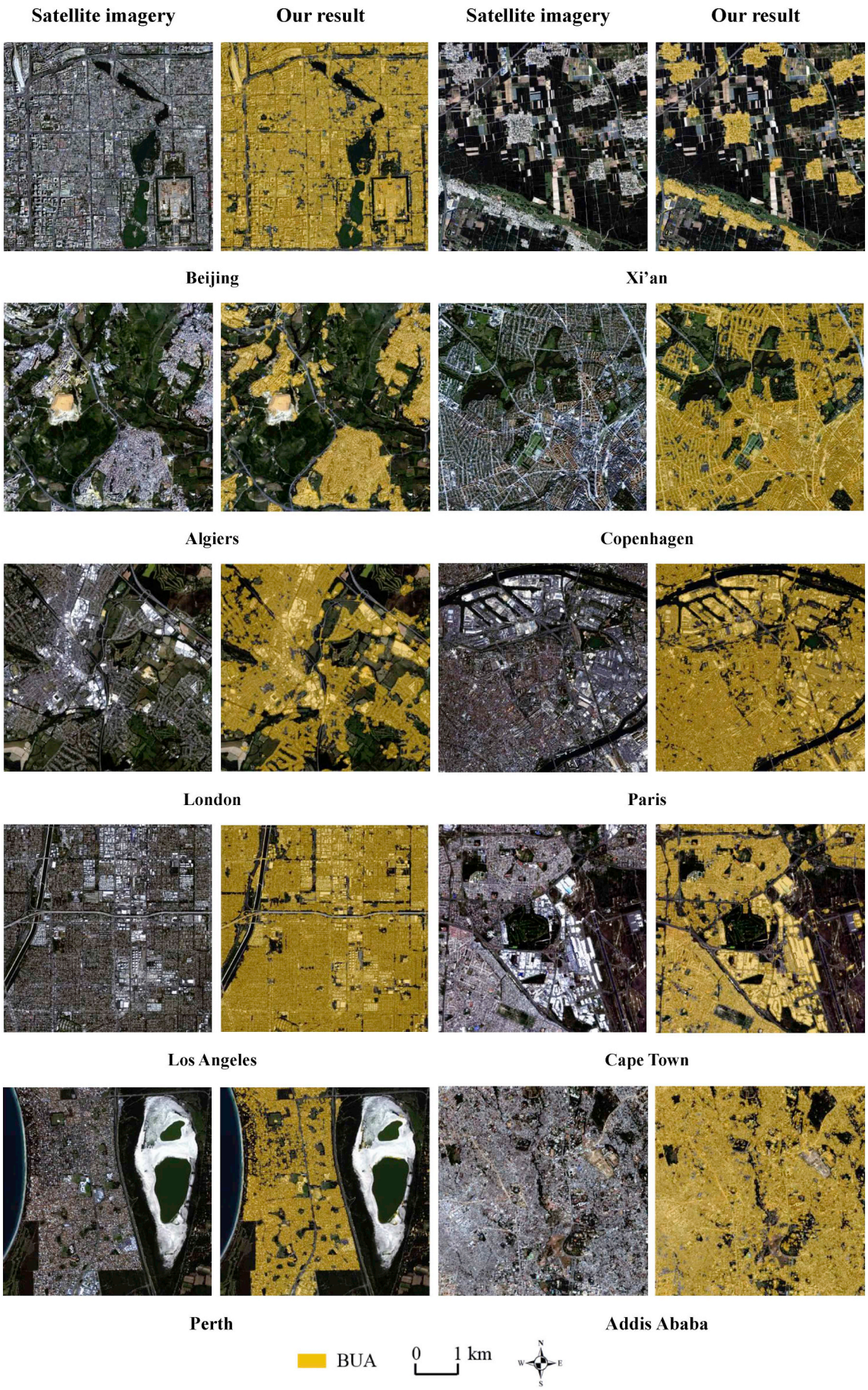

Fig. 4. 5 × 5 km zoom-in regions in some of the test cities, displaying examples of our mapping results.

features (PLA + MABI) for the 40 cities, but for the 5 cities without multi-angle images, only PLA were obtained. The vertical features, include RMABI and NDMABI, were merged with the planar features respectively to generate different BUA results (written as PLA + RMABI and PLA + NDMABI).

For the results generated by the planar features, the OA values ranged from 78.04% to 97.51%. Very satisfactory performances were obtained in 29 test cities, whose OA values were higher than 90%. The best results by using planar features were achieved over Harbin, London, Tokyo and Los Angeles, with F around 0.95. The worst results were from Lhasa and Changsha, whose F values were lower than 0.7. After fusing the vertical features (i.e., RMABI and NDMABI), the OA, F, and PA values increased in most of the test cities, while the UA values may decrease due to the commission errors induced by MABIs. Fig. 5 illustrates the accuracy comparisons by using planar (x-axis) and planar-vertical features (y-axis) in the 40 test cities where multi-view images were available. The general accuracy improvements over the 40 test cities were 1.00% and 0.02 in OA and F, respectively, for RMABI, and 0.81%, and 0.02, in OA and F, respectively, for NDMABI. By focusing on the F scores, 31 and 28 cities had increased by adding the RMABI and NDMABI, respectively. Specifically, the PA values in 10 and 15 cities, have been significantly increased by > 10% after considering RMABI and NDMABI, respectively. Most of these cities (e.g., Changchun, Shanghai, Changsha, Fuzhou, Kunming, and Seoul) exhibit a number of medium/high rise buildings with low local contrast. On the other hand, the UA values in 8 and 10 cities have decreased by > 5% after adding RMABI and NDMABI, respectively. Most of these cities (e.g., Jinan, Lhasa, Chakwal, and Santiago) are in a mountainous environment and the false alarms were mainly caused by topography, e.g., rugged terrain or canyons. The fusion of RMABI and NDMABI achieved similar OA and F values, while in most cases, relatively higher UA and lower PA values were obtained by RMABI. Please notice that since all images were resampled to a uniform spatial resolution of 2.5 m during the pre-processing step, the difference between ZY3–01 and ZY3–02 sensors had little impact to the final result according to our test.

5. Discussion

5.1. Comparison between our result and existing built-up products

To further investigate the performance of the proposed method, we compared our result with two existing built-up products. The recently released GHSL 38 m and GUF 12 m built-up layers were used for this comparison due to their similar definition, high spatial resolution, high accuracies, and reliabilities (Pesaresi et al., 2016; Klotz et al., 2016; Esch et al., 2017; Leyk et al., 2018; Melchiorri et al., 2018). Table 3 compares the definitions, data sources and approaches between the existing two products and our study.

Fig. 6 illustrates the visual difference between the three products by taking Cape Town as an example. In Fig. 6(a), the GHSL, GUF and our result are superimposed on the satellite imagery from bottom to top, respectively. In general, it can be observed that our result and GUF can better distinguish BUA from road networks and soil than GHSL. The zoom-in regions in Fig. 6(b) demonstrate that our result and GUF have similar spatial extent and can reserve more details than GHSL. Compared to GUF, the proposed method had better performance with large buildings as shown in P #2 and P #3. The scattered small houses in rural areas in P #3 were successfully extracted by our method, but partly omitted by GUF. The cropland and bare soil in the south of the city were falsely detected by GHSL.

BUA in rural areas tends to be underestimated when generated from lower resolution images (Klotz et al., 2016; Leyk et al., 2018). Therefore, the quantitative comparison between our results and GHSL under different landscapes was necessary. Since there is no globally consistent rule to separate urban and rural areas, an appropriate approach is to employ existing global products from coarser resolution. For example, Klotz et al. (2016) utilized the Global Rural-Urban Mapping Project's (GRUMP) urban layer to distinguish urban and rural areas, for the comparisons among MOD500, GLOBC, GHSL and GUF. In this study, the MOD500 urban layer was employed to identify urban and rural areas since it had higher spatial resolution and accuracy than GRUMP.

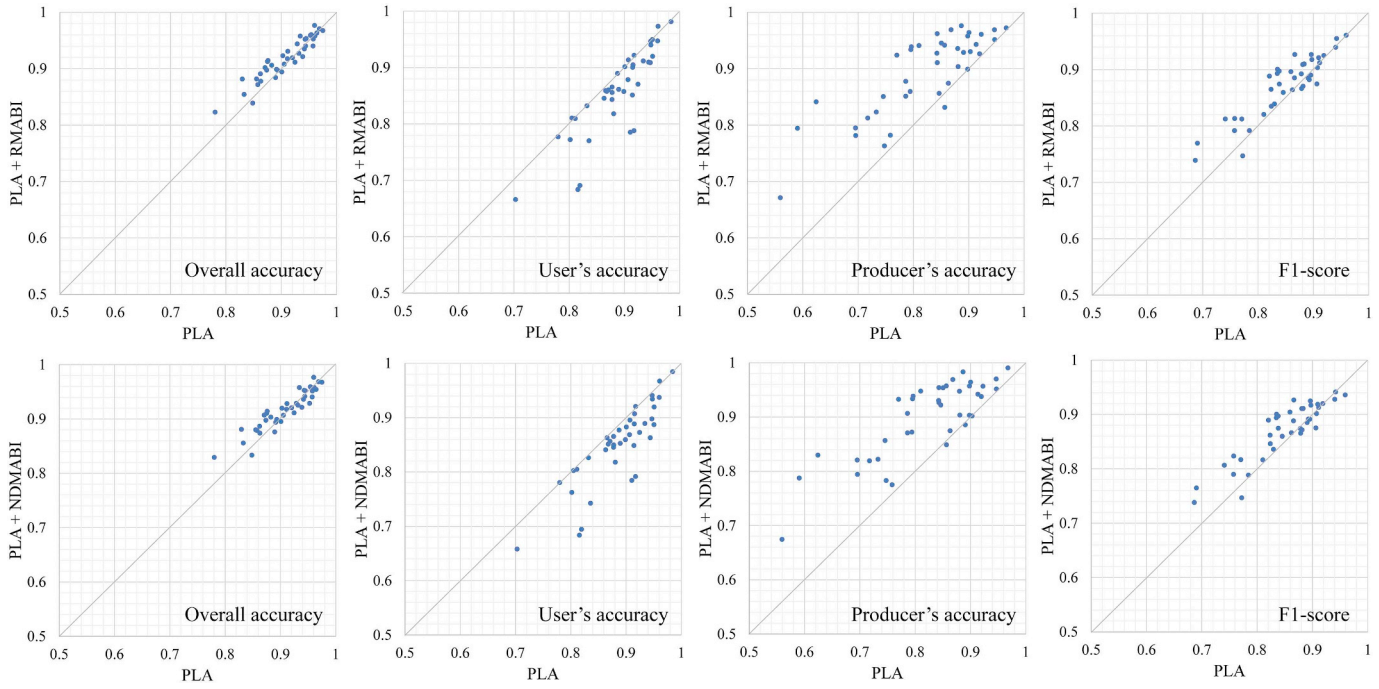

Fig. 5. Comparisons of the accuracies by using the planar features (x-axis) and planar-vertical features (y-axis) in the 40 test cities (with multi-view images available).

Table 3
Summary of the definitions, data sources and approaches of GHSL, GUF and our study.

	Definition of BUA	Primary data source	Approach
GHSL	The union of all the spatial units collected by the specific sensor and containing a building or part of it.	Landsat	Supervised, symbolic machine learning
GUF	Detailed building distribution marked by the presence of vertical structures.	TerraSAR-X/TanDEM-X	Unsupervised, support vector data description
Our study	Detailed spatial delineation of the land surface which is dominantly covered by buildings.	ZY3 multi-view images	Unsupervised, planar-vertical feature fusion

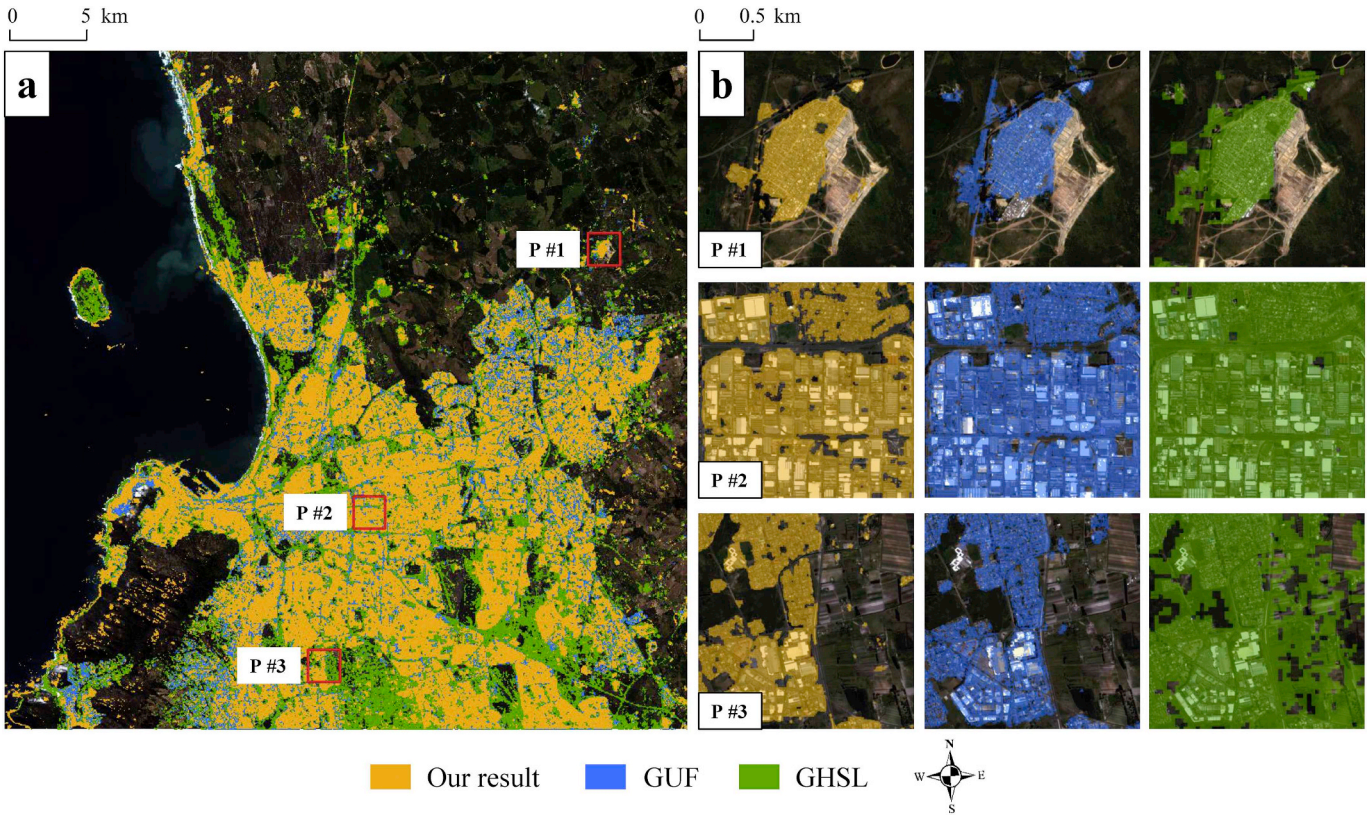

Fig. 6. Comparison between our result, GUF and GHSL: (a) is the ZY3 true color image of Cape Town, overlaid with GHSL, GUF and our result, from bottom to top; (b) is the zoom-in display of the three small patches which are marked in (a) as P #1, P #2 and P #3.

Table 4
Average accuracies of our results and GHSL for all test cities.

	Our result				GHSL			
	OA (%)	UA (%)	PA (%)	F	OA (%)	UA (%)	PA (%)	F
Overall	92.00	86.20	89.14	0.87	84.18	84.06	68.77	0.71
Urban	89.35	90.81	91.80	0.91	78.92	85.46	82.77	0.81
Rural	92.80	81.81	84.85	0.83	85.86	81.51	56.78	0.61

Note that the BUA results, i.e., PLA + RMABI of the 40 cities with multi-view images available and PLA of the 5 cities with only single view image available, were used for this comparison. Table 4 lists the average accuracies of our result and GHSL for all the test cities, and the detailed accuracies of each city are provided in Table A1 in the appendix. In general, our results show consistently higher average accuracies than GHSL in both urban and rural areas. Significant improvements of the PA and F values can be observed in rural regions, indicating that our results had much less omission errors. Fig. 7 illustrates the scatterplots of the four accuracy metrics in different regions, by recording our results in the vertical axis and GHSL in the horizontal axis, respectively. Most of the points lie above the 1:1 diagonal line, implying that our results achieved higher accuracy than GHSL in a majority of the test cities.

In addition, the GUF data of 5 cities (i.e., Beijing, Cape Town, Santiago, Moscow, and Rome) were also applied for quantitative comparison with our results. Because the GUF product is not open access and is currently available only by request from DLR (German Aerospace Center), for comparison, five cities were chosen due to their representativeness for different urban landscapes. As listed in Table 5, the average accuracies of the two products were around 90% in terms of OA and higher than 0.85 in terms of F, indicating satisfactory performances achieved by both products. In general, our results achieved higher or equivalent OA and F values than GUF in all the five cities. Specifically, our results show about 5% ~ 16% higher PA values than GUF in four of the five cities, and approximately the same PA value in Beijing. For the UA values, our results outperform GUF in Beijing and Moscow, while they were less accurate in Cape Town, Santiago and Rome.

Please notice that GHSL and GUF are state-of-the-art global built-up products, and had employed a large set of ancillary data in their training or post-editing steps. It is not reasonable to state that our product was better than GHSL or GUF, since they were derived from very different data sources, and inconsistency can also be induced by different acquisition time between Landsat, TerraSAR-X/TanDEM-X and ZY3 images. However, it can corroborate the effectiveness of our method to extract the BUA by merging the structure, corner, and vertical features based on ZY3 stereo images.

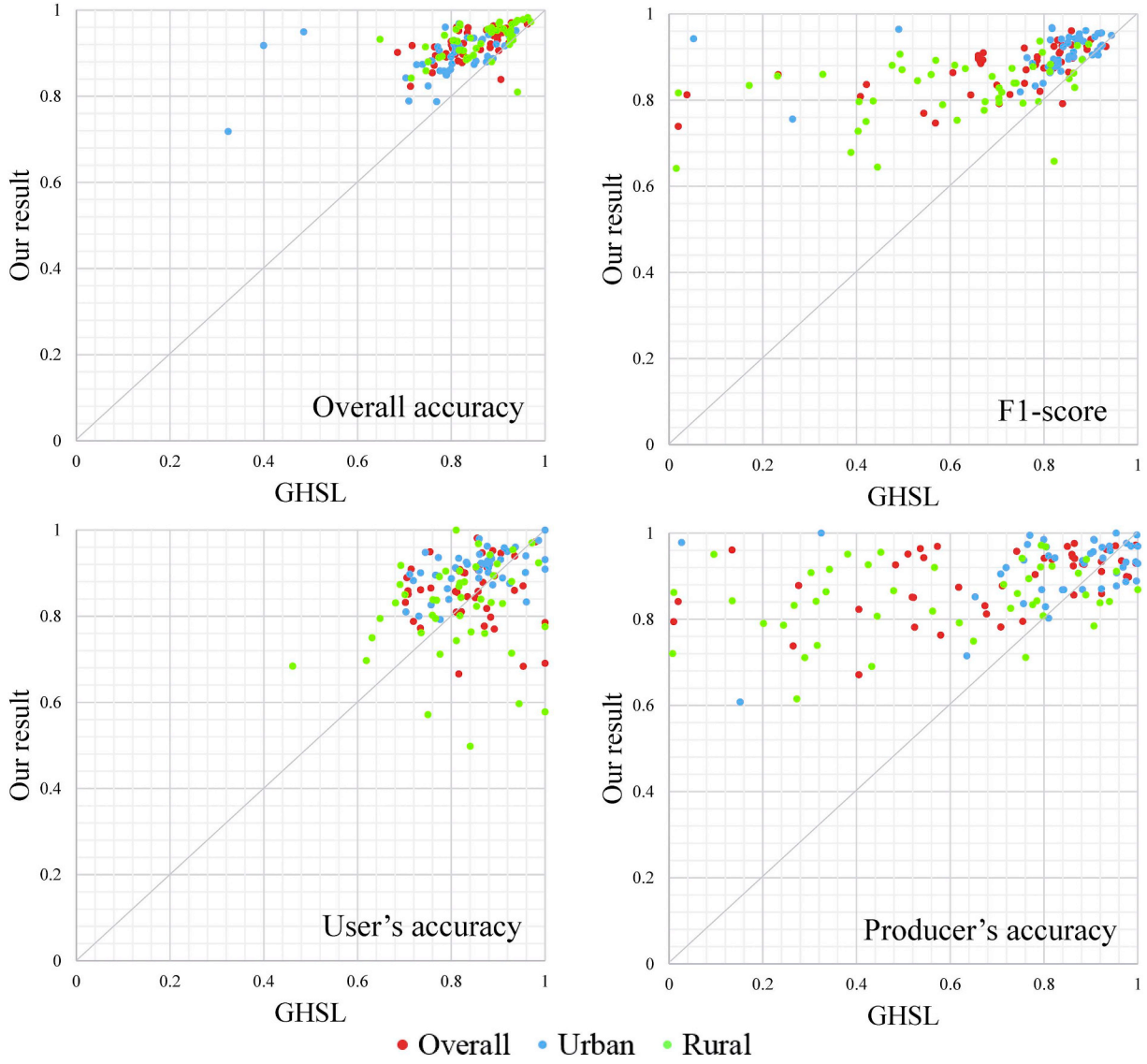

Fig. 7. Comparison of the accuracies between our result (y-axis) and GHSL (x-axis).

Table 5
Accuracies of our results and GUF in 5 representative cities.

	Our result				GUF			
	OA (%)	UA (%)	PA (%)	F	OA (%)	UA (%)	PA (%)	F
Beijing	88.19	88.95	85.95	0.87	82.41	80.25	86.43	0.83
Cape Town	94.02	85.12	89.92	0.87	92.17	94.39	74.16	0.83
Santiago	94.02	87.05	95.78	0.91	94.07	91.67	90.43	0.91
Moscow	89.73	86.13	91.06	0.89	84.52	81.88	84.45	0.83
Rome	94.49	90.66	95.08	0.93	91.47	92.00	88.34	0.90
Average	92.09	87.58	91.56	0.89	88.93	88.04	84.76	0.86

5.2. Effects of the features

The MBI, Harris corner, and MABI had different capabilities to extract buildings. We used the city of Changchun as an example, to illustrate the effects of the three features in Fig. 8. The merged building map of the whole area is displayed in the false color composite in Fig. 8 (b), where the MBI, Harris, and RMABI are represented in red, green and blue, respectively. The yellow, magenta and cyan indicate the area covered by two features, and the white indicates the areas that are identified by all the three features simultaneously (see the tricolor legend). Three zoom-in regions from the residential, industrial and rural areas of the city are demonstrated separately, and the proportion of the building pixels extracted by a certain feature in the fused building map is defined as its contribution. In P #1, with various kinds of buildings in the city center, the three features occupy a similar proportion. Note that the dark buildings can be detected by RMABI more effectively. In P #2,

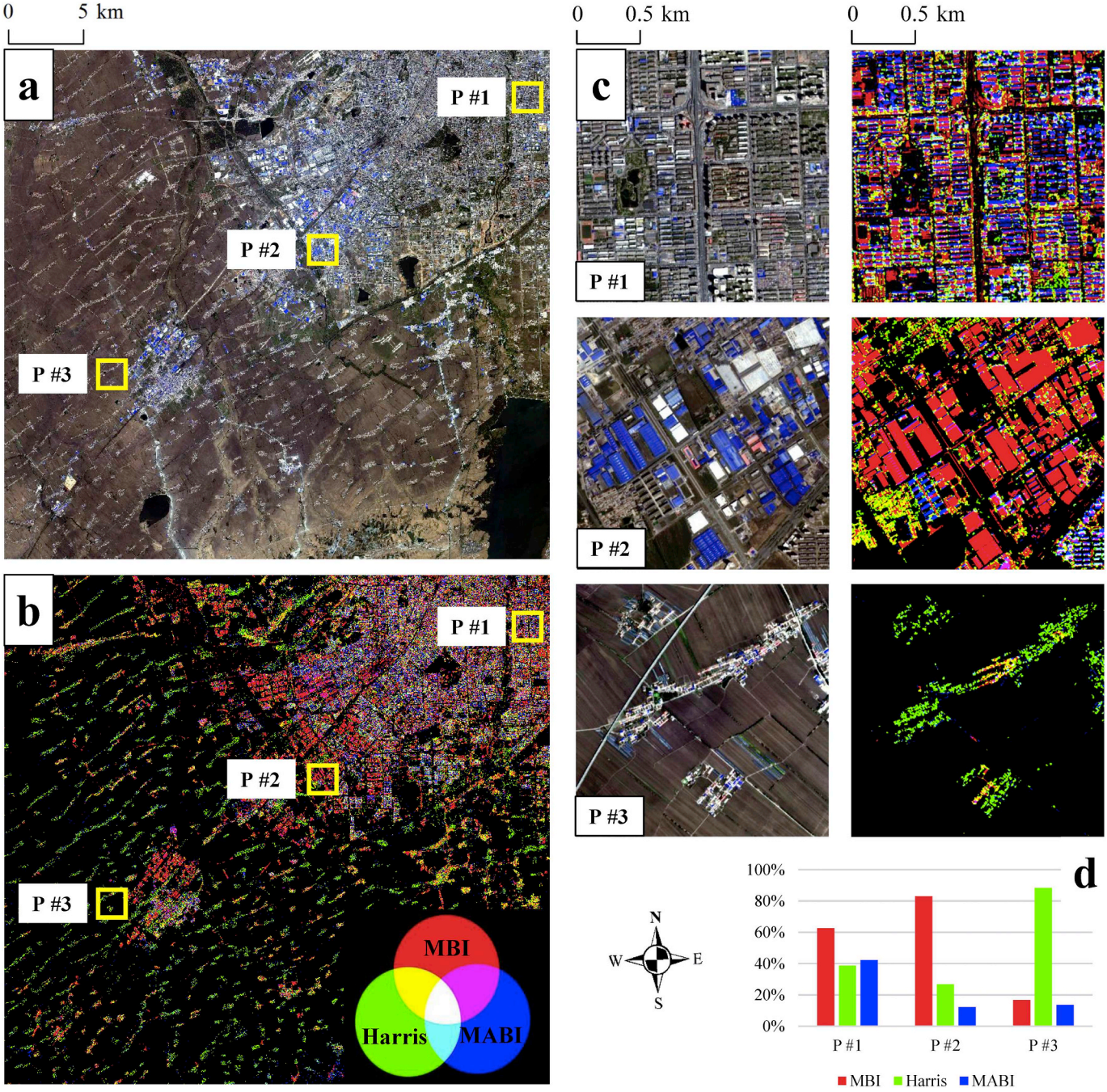

Fig. 8. Demonstration of the feature complementarity: (a) is the true color satellite image of Changchun, China, marked with three small patches as examples; (b) is the false color composite, displaying MBI, Harris and RMABI features in red, green and blue, respectively; (c) shows the zoom-in regions of the three representative patches (called as P #1, P #2 and P #3), which are residential, industrial and rural areas, respectively; (d) presents the contribution of each feature in different patches (defined as the proportion of the building pixels in the fused building map). (For interpretation of the references to color in this figure legend, the reader is referred to the web version of this article.)

located in a peri-urban area with many large and low-rise industrial buildings, MBI plays a vital role in detecting these buildings due to their high brightness and large local contrast. With respect to P #3, dominated by a large number of small houses in a rural area, the Harris feature achieves the optimal performance. This example shows that, in this study, the three features can complement each other and obtain satisfactory results by feature fusion.

The accuracies of the final results of Changchun generated by using one single feature and multi-features were further compared in Fig. 9. Generally, the accuracies of the multi-features (PLA + RMABI) were stably high, but the performance achieved by an individual feature fluctuated. MBI and Harris corner had relatively higher overall accuracies than RMABI. However, RMABI showed the highest UA, indicating that it introduced the least commission error. This phenomenon suggested that RMABI was very appropriate to serve as a complementary feature since it can reduce the omission errors but did

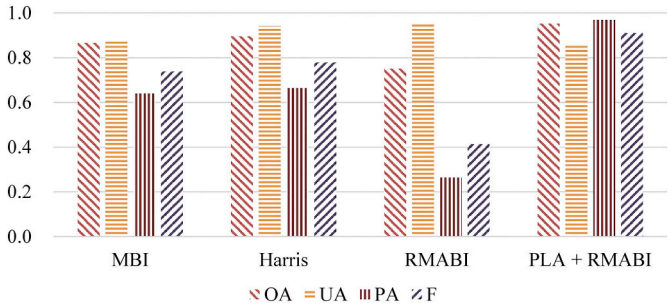

Fig. 9. Accuracies of the results generated by using single feature (written as MBI, Harris, and RMABI, respectively) and the fused features (PLA + RMABI).

Table 6
Average accuracies of the 40 test cities under different landscapes by using RMABI and NDMABI individually.

	RMABI				NDMABI			
	OA (%)	UA (%)	PA (%)	F	OA (%)	UA (%)	PA (%)	F
Overall	76.43	88.42	36.85	0.50	78.22	87.66	41.92	0.54
Urban	65.22	94.48	46.51	0.60	68.17	93.91	51.87	0.63
Rural	81.62	82.05	29.11	0.41	82.87	81.06	33.80	0.45

not induce many false alarms. The OA, PA and F values of the PLA + RMABI were the highest. This result can further support the rationality of the proposed feature fusion strategy.

To thoroughly understand the capabilities of the proposed MABIs for BUA detection under different environments and landscapes, results were generated for all the test cities by using the vertical features alone. The average accuracies of RMABI and NDMABI in the 40 test cities (including urban, rural, and both areas) are reported in Table 6, and the detailed accuracies are listed in Table A1. Generally, the UA values were significantly higher than PA, indicating that the MABIs had less false alarms. The UA, PA and F values in urban areas were much higher than rural areas. This is attributed to the fact that the buildings in rural areas were generally low, and therefore exhibited inconspicuous variations in the multi-view images. With respect to the two different MABIs, although little difference between their accuracies was observed when fused with the planar features as described in Section 4.2, NDMABI performed better than RMABI when they were used individually.

5.3. Effects of post-processing

Post-processing can further improve the precision of the proposed method. Fig. 10 illustrates the removed areas in four example cities by employing the post-processing, which involve trees, croplands, bare soil, and roads. As can be seen from Table 7, the commission errors of the four cities were reduced by 15.58%, 4.81%, 5.29% and 8.66%, respectively. To clearly demonstrate the details and effects of the post-processing (the spectral and shape constraints), three representative areas are displayed in Fig. 11. It can be observed that the spectral constraints can remove the cropland and soil in example #1 by employing the SAVI, and eliminate the bright water areas in example #2 by considering the NDWI. The shape constraint is able to clean the small noise and elongated roads in example #3.

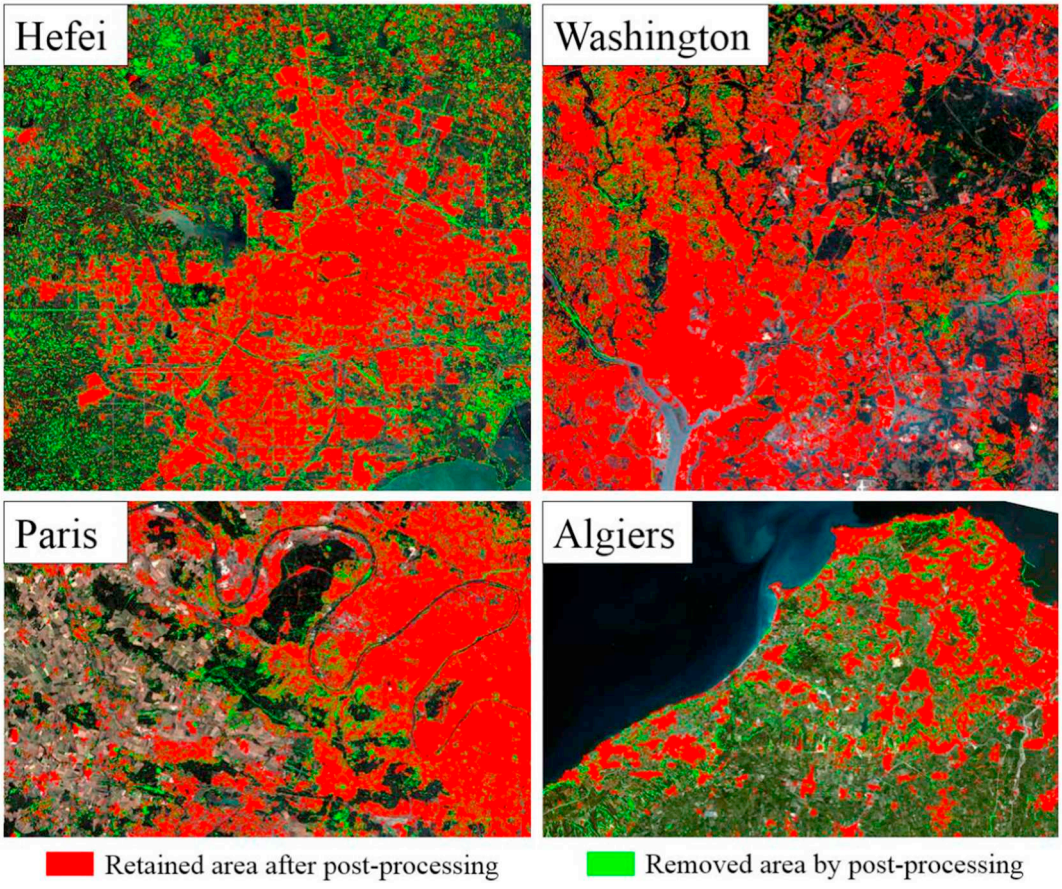

Fig. 10. Examples to show the effects of post-processing. The retained and removed areas after post-processing are superimposed to the true color images.

Table 7
Comparison of BUA extraction accuracies with and without post-processing.

	Hefei		Washington		Paris		Algiers	
	No -post	-post	No -post	-post	No -post	-post	No -post	-post
OA (%)	83.44	91.94	87.61	89.88	89.68	93.07	96.45	97.07
UA (%)	65.37	80.95	81.09	85.90	84.75	90.04	86.06	94.72
PA (%)	98.21	92.63	94.16	92.87	92.29	93.56	98.90	90.37
F	0.78	0.86	0.87	0.89	0.88	0.92	0.92	0.92

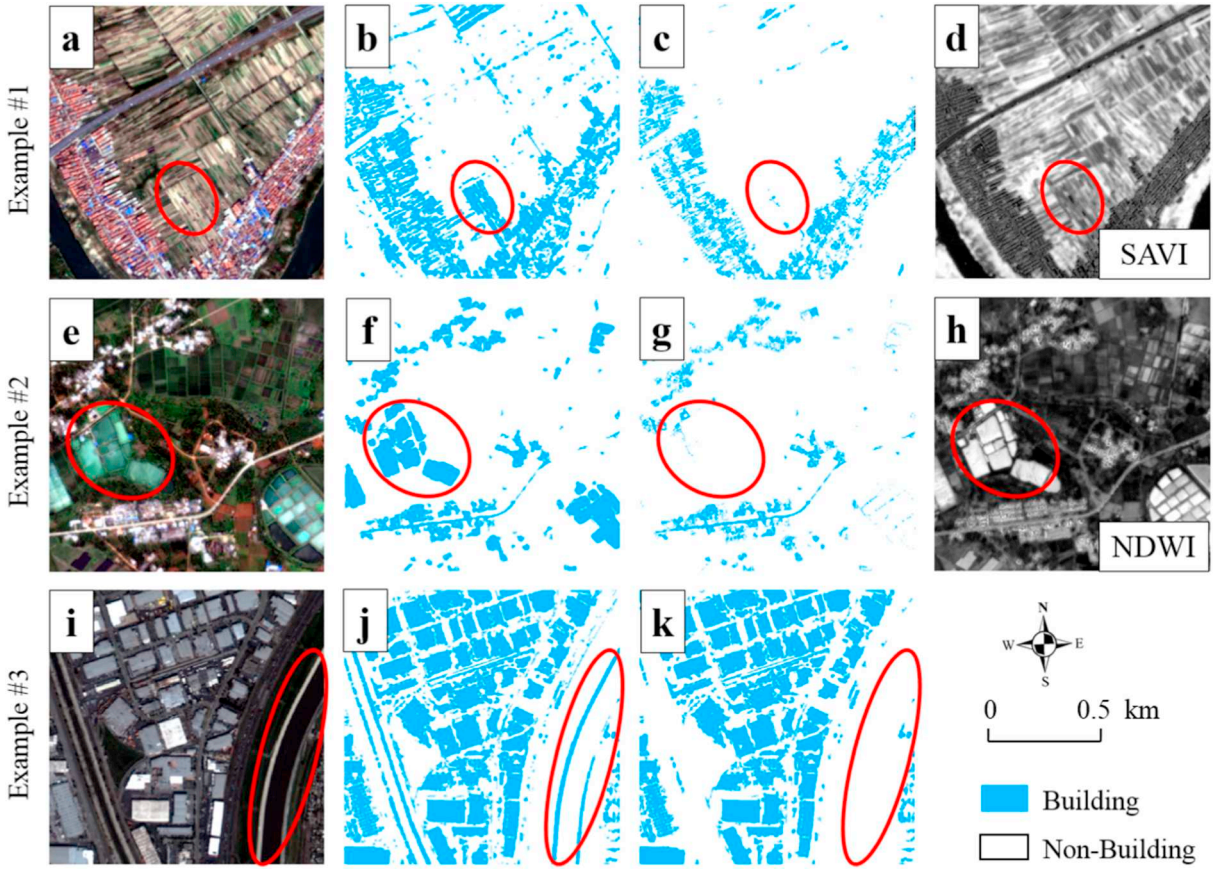

Fig. 11. Examples to show the effects of the spectral and shape constraints: (a~d) example #1 shows the effect of the spectral constraint by using the SAVI index to remove vegetation and soil; (e~h) example #2 illustrates the performance by using the NDWI to remove bright water areas; (i~k) example #3 shows the effect of the shape constraint to remove roads and other noise. Note that (b, f, j) are the candidate buildings before post-processing, and (c, g, k) are the retained buildings after post-processing.

Table 8
Comparison of BUA extraction accuracies with RMABI and DSM.

	PLA + RMABI				PLA + nDSM			
	OA (%)	UA (%)	PA (%)	F	OA (%)	UA (%)	PA (%)	F
Beijing	88.19	88.95	85.95	0.87	87.96	88.00	87.07	0.88
Shanghai	88.17	85.56	92.38	0.89	88.65	86.00	92.61	0.89
Seoul	91.29	85.77	94.09	0.90	91.16	86.04	93.26	0.90
Algiers	97.07	94.72	90.37	0.92	97.96	91.35	99.45	0.95
Paris	93.07	90.04	93.56	0.92	90.80	89.76	87.12	0.88
Average	91.56	89.01	91.27	0.90	91.31	88.23	91.90	0.90

5.4. Comparison of RMABI and nDSM

The normalized DSM (nDSM) is commonly used in urban applications when multi-view images were available, as it describes the height of the off-terrain objects. Therefore, the performances of nDSM and RMABI were compared with five representative cities, i.e., Beijing, Shanghai, Seoul, Algiers and Paris. The DSMs of the five cities were produced from ZY3 multi-view images, by using the semi-global matching (SGM) method (Hirschmuller, 2008). Afterwards, we obtained nDSMs by using morphological top-hat-by-reconstruction (Qin and Fang, 2014; Huang et al., 2017a). Table 8 shows that similar accuracies can be obtained by using RMABI and nDSM when fused with the planar features. However, considering that the computation time and complexity of MABI was far less than nDSM, the former was therefore focused on in this research for large scale BUA extraction. In particular, Fig. 12 demonstrates an example of nDSM and RMABI, respectively, in a dense urban area of Shanghai. It can be seen that the high buildings marked by red circles were better extracted by RMABI, and the errors occurred in nDSM can be attributed to the matching errors derived from the large disparity and occlusion of high-rise buildings.

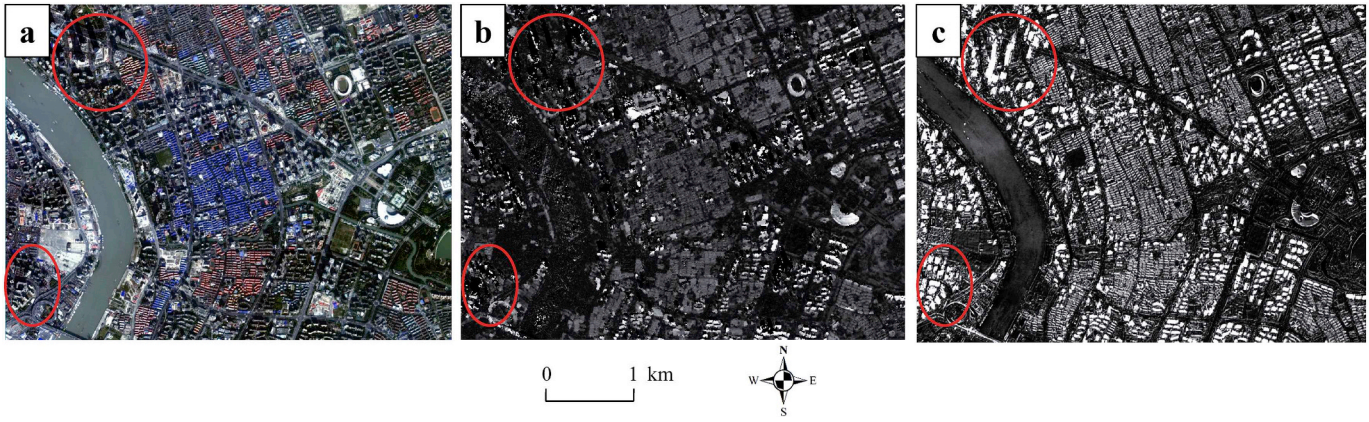

Fig. 12. (a) the ZY3 true color image in Shanghai, China; (b) nDSM and (c) RMABI generated from ZY3 multi-view images, respectively.

6. Conclusions

In this research, we developed a novel planar-vertical feature fusion method for automated BUA extraction from ZY3 multi-view high-resolution images. Totally 45 representative cities around the world were selected as test areas with the images acquired by the ZY3 satellite constellation. Among them, 40 cities had multi-view images available, and 5 cities had only nadir-view images. The proposed method can effectively and explicitly distinguish BUA from other ground objects (e.g., bare soil, parks, main roads, rivers) by employing the three features, i.e., Morphological Building Index (MBI), Harris corner detector, and Multi-angular Built-up Index (MABI), to describe different building characteristics from the structural, corner response, and vertical properties, respectively. The concluding remarks were summarized as the following.

1) The MBI was capable of retrieving the original shape and size of buildings, therefore efficient to extract large buildings (e.g., factories and commercial buildings). The Harris corner highlighted the corners of buildings and was sensitive to small houses in rural areas. Experimental results show that the fusion of the two planar features can detect BUA with satisfactory accuracies in most of the test cities, and obtained the average OA, UA, PA and F values of 91.12%, 88.85%, 82.82% and 0.85, respectively. Omission errors of the planar features were mainly derived from the built-up areas with low brightness and local contrast.
2) When multi-view images were available, the novel multi-angular built-up indices (MABIs), i.e., RMABI and NDMABI, were proposed to further complement the planar features. Accuracies of the results generated by the vertical features alone were relatively low (with average F of 0.50 and 0.54 for RMABI and NDMABI, respectively), as they were subject to omissions of low-rise buildings. However, the MABIs can serve as effective complements to the planar features, since the fusion of planar-vertical features improved the OA, PA and F values in most of the test cities (e.g., Shanghai, Changsha, Guangzhou, Shenzhen, Seoul). These cities exhibited a large number of medium/high rise buildings with low brightness or local contrast. It was found that MABIs were effective to complement the planar features when dealing with such urban scenes. The average OA, UA, PA and F values of the final results by fusing the planar-vertical features were 92.00%, 86.20%, 89.14% and 0.87 for the RMABI, and 91.83%, 85.51%, 89.62% and 0.87 for the NDMABI, respectively.
3) Our results were compared with two state-of-the-art global BUA products, GHSL (Global Human Settlement Layer) and Global Urban Footprint (GUF). The average increments of OA, UA, PA and F values obtained by our results were 7.82%, 2.14%, 20.37% and 0.16, respectively, compared to GHSL. Particularly, our results achieved more consistent accuracies under different landscapes (urban and rural areas), with the PA 28.08% higher than GHSL in rural areas. Compared to GUF, our results achieved similar or higher OA and F values. These results further corroborated the effectiveness of our method, especially considering that no ancillary data was used during our experiments.
4) The results indicated that the proposed method has the potential to be applied for global mapping of high-resolution built-up areas, which can provide a more accurate data source for the global population, economy, resource and environment studies. In practical use, different strategies can be adopted according to the scene characteristics and user's needs. Specifically, our results show that MBI and MABI are more effective in urban and peri-urban areas, while the corner feature is more suitable for rural areas. MABI and Harris corner features have less commission errors, and hence can be considered when UA is more important than PA. If high PA is pursued, the feature fusion is recommended, since in such cases, MABIs are able to complement the planar features and produce the least omissions.
5) The errors of our results mainly stemmed from greenhouse, parking lot, rough soil surface, which may be falsely detected by the planar features, since they exhibited similar characteristics to buildings; drastic topography change (e.g., rugged terrain or canyons) also induced false alarms by the vertical features due to their distinct angular variations. These kinds of errors can be reduced by considering additional information sources (e.g., Volunteered Geographic Information, Digital Elevation Model) in future research.

Acknowledgments

The authors would like to thank Dr. Jiayi Li, from Wuhan University, P.R. China, for providing great help and advice on feature design of the multi-angular built-up indices (MABIs). This research was supported by the National Natural Science Foundation of China under Grant 41771360, the National Program for Support of Top-notch Young Professionals, the Hubei Provincial Natural Science Foundation of China under Grant 2017CFA029, and the National Key R&D Program of China under Grant 2016YFB0501403.

Appendix A

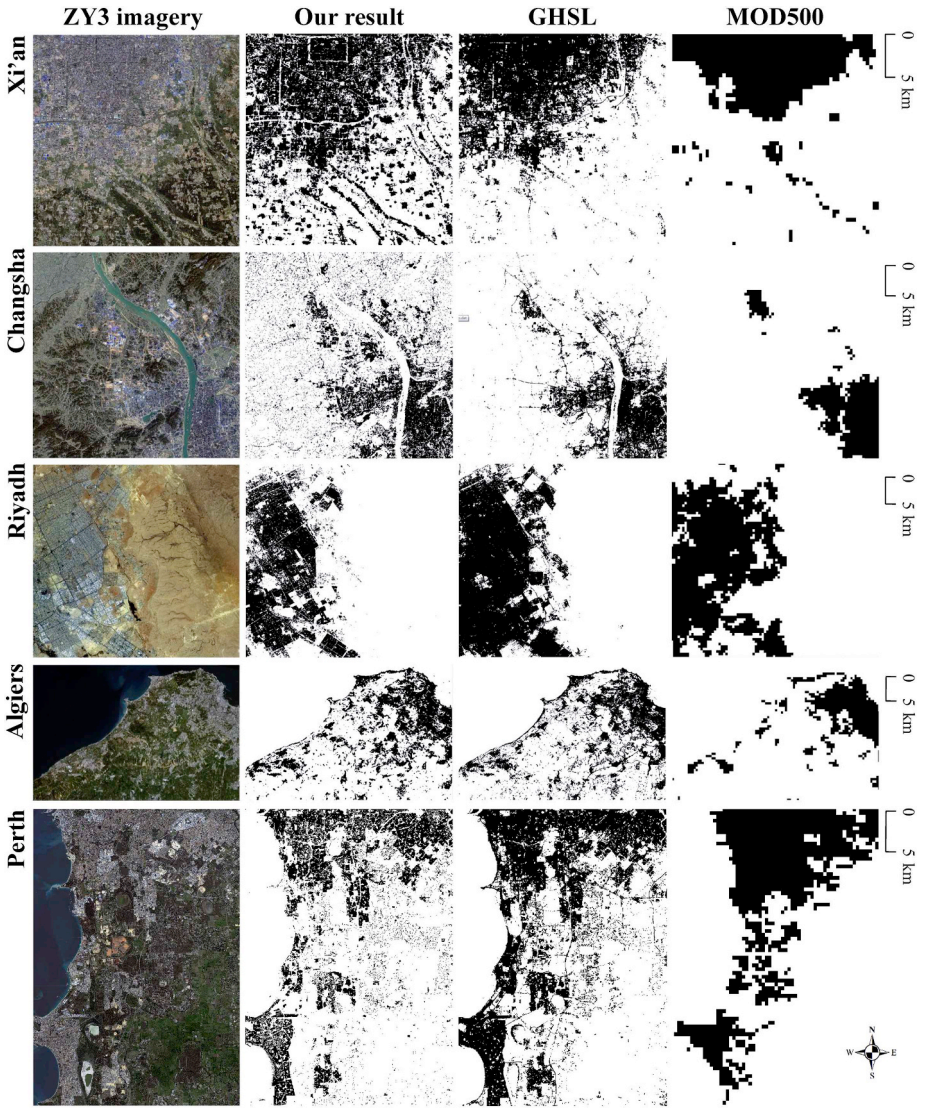

Fig. A1. Built-up areas (in black) in five representative cities from our results, GHSL, and MOD500.

Table A1
Accuracies of our results and GHSL of the 45 test cities under different landscapes.

		Overall				Urban				Rural			
		OA (%)	UA (%)	PA (%)	F	OA (%)	UA (%)	PA (%)	F	OA (%)	UA (%)	PA (%)	F
Beijing	PLA	85.53	88.75	79.43	0.84	84.32	91.11	81.38	0.86	86.29	86.42	74.07	0.80
	RMABI	67.79	93.09	37.91	0.54	67.62	94.95	49.18	0.65	67.96	85.42	18.99	0.31
	NDMABI	72.70	92.74	48.56	0.64	72.66	93.13	59.53	0.73	72.84	91.43	29.80	0.45
	PLA + RMABI	88.19	88.95	85.95	0.87	87.40	89.77	88.88	0.89	88.97	87.36	80.80	0.84
	PLA + NDMABI	87.99	87.71	87.20	0.87	87.34	89.05	89.97	0.90	88.70	85.16	82.33	0.84
	GHSL	75.62	70.50	92.30	0.80	73.82	71.10	99.71	0.83	77.34	69.04	79.82	0.74
Harbin	PLA	96.45	93.42	94.66	0.94	93.96	94.12	95.36	0.95	97.67	93.36	95.71	0.95
	RMABI	84.42	93.36	53.09	0.68	72.44	94.59	56.14	0.70	88.79	92.41	52.29	0.67
	NDMABI	86.45	88.82	64.12	0.74	76.73	93.60	64.69	0.77	90.07	85.47	65.51	0.74
	PLA + RMABI	96.33	91.16	96.90	0.94	93.50	92.05	96.69	0.94	97.22	90.45	97.18	0.94
	PLA + NDMABI	95.44	88.92	97.02	0.93	92.46	90.50	96.73	0.94	96.35	87.67	97.34	0.92
	GHSL	88.99	80.94	84.97	0.83	84.80	83.42	92.39	0.88	90.32	78.80	79.40	0.79

(*continued on next page*)

Table A1 (*continued*)

		Overall				Urban				Rural			
		OA (%)	UA (%)	PA (%)	F	OA (%)	UA (%)	PA (%)	F	OA (%)	UA (%)	PA (%)	F
Changchun	PLA	94.31	89.90	86.81	0.88	89.82	94.29	91.87	0.93	95.22	89.40	85.21	0.87
	RMABI	75.09	95.65	26.34	0.41	71.07	98.63	61.97	0.76	76.05	93.18	15.82	0.27
	NDMABI	74.71	95.54	25.49	0.40	70.16	98.61	60.71	0.75	75.73	92.94	15.17	0.26
	PLA + RMABI	95.22	85.75	96.91	0.91	93.24	91.38	100.00	0.95	95.50	83.70	95.56	0.89
	PLA + NDMABI	95.28	85.94	96.92	0.91	93.25	91.38	100.00	0.95	95.57	83.96	95.58	0.89
	GHSL	81.58	80.88	57.25	0.67	86.65	87.93	95.37	0.91	81.01	76.85	45.18	0.57
Hohhot	PLA	93.18	87.10	94.70	0.91	92.75	91.88	98.54	0.95	93.45	84.19	91.34	0.88
	RMABI	76.64	98.17	39.04	0.56	77.46	100.00	64.90	0.79	76.66	95.35	23.61	0.38
	NDMABI	80.61	95.93	49.86	0.66	81.04	98.60	72.17	0.83	80.90	92.91	35.91	0.52
	PLA + RMABI	92.71	86.01	95.15	0.90	91.94	90.15	99.50	0.95	92.94	82.97	91.59	0.87
	PLA + NDMABI	92.52	85.65	95.18	0.90	91.92	90.15	99.51	0.95	92.71	82.37	91.64	0.87
	GHSL	79.95	93.45	50.96	0.66	81.57	95.80	76.97	0.85	80.34	90.91	34.22	0.50
Taiyuan	PLA	84.84	70.30	88.68	0.78	88.81	90.77	91.48	0.91	83.58	54.04	86.52	0.67
	RMABI	78.71	80.39	41.14	0.54	63.65	95.00	43.88	0.60	85.14	66.35	39.47	0.49
	NDMABI	80.30	77.29	50.17	0.61	68.17	91.34	52.81	0.67	84.98	62.90	47.32	0.54
	PLA + RMABI	83.90	66.60	97.62	0.79	91.01	88.73	98.37	0.93	80.96	49.82	96.82	0.66
	PLA + NDMABI	83.34	65.81	98.32	0.79	90.36	87.56	98.91	0.93	80.34	49.30	97.66	0.66
	GHSL	90.56	81.57	86.46	0.84	80.85	80.00	90.74	0.85	94.11	84.03	80.34	0.82
Yinchuan	PLA	91.11	78.01	92.27	0.85	92.26	92.96	96.15	0.95	91.24	74.61	92.22	0.82
	RMABI	75.02	89.90	20.06	0.33	43.77	93.33	27.18	0.42	78.69	89.29	19.12	0.31
	NDMABI	74.45	90.11	18.54	0.31	43.06	93.33	25.88	0.41	78.05	89.47	17.44	0.29
	PLA + RMABI	91.75	77.72	96.09	0.86	94.95	93.15	100.00	0.96	91.47	74.32	95.06	0.83
	PLA + NDMABI	91.77	78.05	95.69	0.86	94.96	93.15	100.00	0.96	91.48	74.70	94.57	0.83
	GHSL	71.63	87.04	13.44	0.23	48.51	100.00	32.46	0.49	74.47	81.08	9.57	0.17
Lanzhou	PLA	90.53	91.56	75.84	0.83	84.60	93.31	77.81	0.85	97.23	80.77	82.22	0.81
	RMABI	70.64	85.90	16.52	0.28	53.75	96.72	19.25	0.32	90.09	47.06	12.40	0.20
	NDMABI	69.86	91.23	14.14	0.24	51.59	97.78	15.83	0.27	90.81	66.67	14.01	0.23
	PLA + RMABI	90.80	90.48	78.21	0.84	85.86	93.46	80.26	0.86	96.67	76.36	83.22	0.80
	PLA + NDMABI	90.68	90.71	77.50	0.84	85.47	93.41	79.56	0.86	96.85	77.78	83.07	0.80
	GHSL	86.20	81.71	70.76	0.76	79.41	81.55	80.98	0.81	92.90	84.21	26.68	0.41
Xi'an	PLA	87.07	94.75	78.62	0.86	79.99	93.43	79.56	0.86	91.69	95.84	81.95	0.88
	RMABI	60.02	96.67	33.05	0.49	61.75	97.04	53.13	0.69	60.21	96.30	22.02	0.36
	NDMABI	68.88	95.97	47.64	0.64	73.25	95.91	69.42	0.81	68.19	96.02	35.21	0.52
	PLA + RMABI	90.19	94.65	85.12	0.90	84.94	93.36	86.87	0.90	93.22	95.43	86.38	0.91
	PLA + NDMABI	90.71	94.08	87.06	0.90	85.46	91.91	89.25	0.91	93.45	95.44	87.46	0.91
	GHSL	68.51	90.57	51.88	0.66	78.89	88.60	84.20	0.86	64.78	93.14	33.49	0.49
Zhengzhou	PLA	83.28	86.33	69.58	0.77	79.71	88.61	77.13	0.82	85.42	83.13	64.28	0.73
	RMABI	80.27	92.10	53.04	0.67	74.59	94.44	60.46	0.74	83.61	89.15	47.83	0.62
	NDMABI	81.46	91.78	57.96	0.71	77.42	94.71	65.87	0.78	83.91	88.06	52.27	0.66
	PLA + RMABI	85.44	84.54	78.15	0.81	84.92	88.84	86.87	0.88	85.91	79.47	71.09	0.75
	PLA + NDMABI	85.57	84.09	79.42	0.82	85.78	88.99	88.34	0.89	85.60	78.35	71.99	0.75
	GHSL	75.93	83.45	52.38	0.64	78.98	85.84	79.51	0.83	74.57	76.62	28.96	0.42
Jinan	PLA	92.47	88.06	90.05	0.89	90.71	94.12	92.12	0.93	93.42	83.91	91.16	0.87
	RMABI	79.06	83.60	57.06	0.68	73.58	93.10	68.74	0.79	80.85	75.58	51.37	0.61
	NDMABI	79.50	83.18	58.36	0.69	73.93	93.10	69.47	0.80	81.48	75.27	53.27	0.62
	PLA + RMABI	91.15	81.80	96.40	0.89	91.45	90.20	98.51	0.94	90.68	76.01	95.11	0.84
	PLA + NDMABI	91.12	81.80	96.42	0.89	91.45	90.20	98.52	0.94	90.64	76.01	95.15	0.85
	GHSL	80.23	87.54	53.61	0.66	77.09	87.86	79.92	0.84	81.64	87.12	38.10	0.53
Hefei	PLA	92.02	81.11	91.98	0.86	82.22	83.53	89.97	0.87	92.58	80.00	91.46	0.85
	RMABI	81.00	98.80	36.06	0.53	73.80	100.00	60.65	0.76	82.19	98.31	30.52	0.47
	NDMABI	83.41	96.48	43.63	0.60	80.13	96.67	71.79	0.82	83.98	96.40	36.94	0.53
	PLA + RMABI	91.94	80.95	92.63	0.86	84.26	83.91	93.71	0.89	92.75	80.13	92.66	0.86
	PLA + NDMABI	92.07	80.49	93.77	0.87	86.32	84.27	96.68	0.90	92.63	79.43	93.12	0.86
	GHSL	80.01	81.06	48.32	0.61	70.29	79.45	75.68	0.78	81.31	81.82	42.48	0.56
Shanghai	PLA	82.95	87.78	77.01	0.82	81.83	87.04	79.85	0.83	86.58	86.70	78.04	0.82
	RMABI	74.79	96.92	49.99	0.66	76.84	98.48	61.16	0.75	72.83	92.55	30.90	0.46
	NDMABI	78.06	95.09	57.99	0.72	80.14	96.27	68.62	0.80	75.96	91.96	39.52	0.55
	PLA + RMABI	88.17	85.56	92.38	0.89	87.51	86.38	94.21	0.90	88.96	83.94	89.44	0.87
	PLA + NDMABI	88.08	84.99	93.27	0.89	87.19	85.65	94.88	0.90	89.14	83.71	90.73	0.87
	GHSL	81.43	81.22	86.25	0.84	80.14	79.17	92.56	0.85	83.29	86.29	76.74	0.81
Wuhan	PLA	85.75	91.75	74.77	0.82	83.38	91.44	80.84	0.86	87.66	92.42	69.92	0.80
	RMABI	60.47	96.97	24.50	0.39	56.59	97.83	34.80	0.51	62.76	95.89	16.16	0.28
	NDMABI	66.77	97.10	34.54	0.51	66.14	98.48	47.56	0.64	67.15	95.41	23.88	0.38
	PLA + RMABI	87.19	92.15	76.31	0.83	85.86	92.14	83.63	0.88	87.98	92.16	69.03	0.79
	PLA + NDMABI	87.87	92.06	78.28	0.85	86.60	92.21	85.04	0.88	88.66	91.94	71.60	0.81
	GHSL	76.33	88.19	57.94	0.70	78.40	86.90	75.62	0.81	75.05	89.78	43.24	0.58
Changsha	PLA	86.24	90.08	55.96	0.69	78.64	93.24	69.07	0.79	87.65	88.83	53.19	0.67
	RMABI	79.02	94.67	32.51	0.48	75.82	95.52	61.88	0.75	79.65	93.98	25.06	0.40
	NDMABI	80.85	93.14	39.35	0.55	81.46	93.59	73.33	0.82	80.89	92.78	30.66	0.46
	PLA + RMABI	89.10	90.14	67.13	0.77	88.18	92.22	86.91	0.89	89.27	89.18	61.50	0.73
	PLA + NDMABI	88.65	88.28	67.44	0.76	87.63	91.21	87.38	0.89	88.83	86.93	61.72	0.72
	GHSL	78.94	82.56	40.50	0.54	85.25	88.17	88.21	0.88	78.08	77.45	27.27	0.40

(*continued on next page*)

Table A1 (*continued*)

		Overall				Urban				Rural			
		OA (%)	UA (%)	PA (%)	F	OA (%)	UA (%)	PA (%)	F	OA (%)	UA (%)	PA (%)	F
Fuzhou	PLA	93.43	87.77	79.64	0.84	92.69	95.65	87.85	0.92	94.01	85.65	78.60	0.82
	RMABI	85.13	88.57	42.74	0.58	80.21	100.00	58.11	0.74	86.37	84.73	39.11	0.54
	NDMABI	82.85	90.14	33.22	0.49	75.90	100.00	48.11	0.65	84.36	86.54	29.72	0.44
	PLA + RMABI	95.78	86.54	93.87	0.90	96.84	94.81	98.53	0.97	95.65	83.83	92.12	0.88
	PLA + NDMABI	95.78	86.54	93.85	0.90	96.84	94.81	98.52	0.97	95.66	83.83	92.09	0.88
	GHSL	89.93	75.62	81.70	0.79	81.63	74.44	90.60	0.82	91.14	76.07	79.25	0.78
Guangzhou	PLA	87.37	90.65	85.64	0.88	85.76	92.88	84.11	0.88	90.42	87.94	89.51	0.89
	RMABI	72.87	91.76	55.10	0.69	73.73	95.30	60.92	0.74	71.72	83.96	43.76	0.58
	NDMABI	78.97	90.05	68.35	0.78	80.36	93.99	73.19	0.82	77.45	82.55	58.86	0.69
	PLA + RMABI	89.76	87.86	94.16	0.91	90.16	90.62	94.24	0.92	89.51	83.18	94.16	0.88
	PLA + NDMABI	89.75	86.86	95.73	0.91	89.80	89.09	95.61	0.92	89.88	83.04	96.05	0.89
	GHSL	82.46	86.74	80.04	0.83	80.67	85.92	82.33	0.84	84.70	88.48	75.32	0.81
Shenzhen	PLA	88.27	80.51	84.26	0.82	84.88	79.72	87.31	0.83	90.41	81.99	83.40	0.83
	RMABI	83.27	96.72	49.30	0.65	77.56	92.86	52.12	0.67	86.00	99.12	47.52	0.64
	NDMABI	85.05	95.19	56.07	0.71	78.96	89.16	58.08	0.70	87.85	99.20	54.84	0.71
	PLA + RMABI	90.62	81.04	92.74	0.86	87.39	79.25	95.69	0.87	92.03	82.30	90.69	0.86
	PLA + NDMABI	90.34	80.26	93.04	0.86	86.48	77.78	95.63	0.86	92.03	82.02	91.26	0.86
	GHSL	90.10	82.14	88.56	0.85	84.86	77.63	90.50	0.84	92.40	85.38	87.33	0.86
Haikou	PLA	94.71	89.38	73.79	0.81	78.73	95.87	71.50	0.82	93.53	94.25	79.02	0.86
	RMABI	/	/	/	/	/	/	/	/	/	/	/	/
	NDMABI	/	/	/	/	/	/	/	/	/	/	/	/
	PLA + RMABI	/	/	/	/	/	/	/	/	/	/	/	/
	PLA + NDMABI	/	/	/	/	/	/	/	/	/	/	/	/
	GHSL	83.40	89.19	26.47	0.41	76.87	91.30	63.52	0.75	84.06	88.24	20.14	0.33
Kunming	PLA	87.61	94.79	74.57	0.83	73.50	80.28	76.42	0.78	80.63	85.71	65.79	0.74
	RMABI	66.90	96.41	28.74	0.44	54.41	97.10	34.10	0.50	75.12	94.74	20.06	0.33
	NDMABI	70.24	95.34	36.08	0.52	58.95	95.68	41.46	0.58	77.64	94.59	27.10	0.42
	PLA + RMABI	91.45	93.99	85.06	0.89	87.33	95.04	85.19	0.90	94.15	92.39	84.17	0.88
	PLA + NDMABI	91.42	93.42	85.68	0.89	87.43	94.41	85.98	0.90	94.01	91.89	84.40	0.88
	GHSL	76.40	93.51	52.15	0.67	72.58	91.95	65.29	0.76	78.53	98.61	31.37	0.48
Chengdu	PLA	78.04	83.23	69.54	0.76	78.40	80.00	76.21	0.78	87.94	78.95	71.15	0.75
	RMABI	75.88	91.39	55.12	0.69	80.24	90.10	76.15	0.83	73.86	92.86	41.11	0.57
	NDMABI	78.64	89.24	63.42	0.74	82.02	87.68	82.56	0.85	77.03	90.91	50.50	0.65
	PLA + RMABI	82.30	83.21	79.50	0.81	78.88	81.01	87.07	0.84	84.21	85.02	74.91	0.80
	PLA + NDMABI	82.94	82.62	82.07	0.82	78.87	80.00	88.88	0.84	85.12	84.80	77.99	0.81
	GHSL	71.29	70.21	75.45	0.73	70.93	70.31	92.25	0.80	71.44	70.10	64.96	0.67
Chongqing	PLA	86.29	80.19	71.75	0.76	89.62	94.19	90.04	0.92	90.42	72.50	49.95	0.59
	RMABI	81.83	85.78	46.64	0.60	77.65	87.50	64.57	0.74	82.62	84.85	40.26	0.55
	NDMABI	84.58	84.68	58.17	0.69	82.32	88.61	75.04	0.81	85.06	82.84	52.01	0.64
	PLA + RMABI	87.79	77.22	81.24	0.79	82.39	80.00	86.85	0.83	88.82	76.15	79.18	0.78
	PLA + NDMABI	87.38	76.23	81.93	0.79	81.24	78.43	86.92	0.82	88.55	75.38	80.11	0.78
	GHSL	82.29	73.40	67.71	0.70	75.05	73.08	83.93	0.78	83.67	73.56	61.92	0.67
Lhasa	PLA	90.09	81.95	59.06	0.69	94.79	96.20	95.14	0.96	93.47	76.47	86.91	0.81
	RMABI	83.07	63.77	49.03	0.55	79.78	93.06	73.00	0.82	83.28	48.15	42.12	0.45
	NDMABI	83.72	65.22	49.48	0.56	80.54	94.37	73.25	0.82	84.07	50.00	43.01	0.46
	PLA + RMABI	89.44	69.07	79.44	0.74	91.77	90.91	97.83	0.94	88.47	57.81	72.04	0.64
	PLA + NDMABI	89.53	69.44	78.75	0.74	91.47	91.67	96.59	0.94	88.84	58.33	72.31	0.65
	GHSL	76.61	100.00	0.99	0.02	39.94	100.00	2.69	0.05	83.18	100.00	0.77	0.02
Urumchi	PLA	94.17	87.76	91.36	0.90	92.71	98.31	90.57	0.94	92.46	100.00	81.74	0.90
	RMABI	83.40	90.58	42.45	0.58	65.10	99.00	43.24	0.60	90.03	81.32	44.05	0.57
	NDMABI	82.62	91.11	39.10	0.55	63.42	98.96	40.42	0.57	89.54	82.14	39.83	0.54
	PLA + RMABI	93.49	84.31	94.29	0.89	96.05	96.26	97.36	0.97	92.19	71.18	90.81	0.80
	PLA + NDMABI	93.62	84.55	94.22	0.89	96.04	96.26	97.33	0.97	92.40	71.60	90.67	0.80
	GHSL	84.42	85.09	54.35	0.66	78.72	87.65	76.46	0.82	86.30	77.59	30.28	0.44
Tokyo	PLA	92.88	98.44	90.29	0.94	88.30	90.39	86.98	0.89	87.86	80.52	71.87	0.76
	RMABI	54.72	97.40	19.32	0.32	53.12	97.24	19.91	0.33	65.78	100.00	7.40	0.14
	NDMABI	48.95	98.82	9.75	0.18	47.17	98.80	10.11	0.18	61.38	100.00	3.24	0.06
	PLA + RMABI	94.39	98.13	93.01	0.96	94.29	97.98	93.35	0.96	94.81	100.00	86.86	0.93
	PLA + NDMABI	92.88	98.44	90.20	0.94	92.81	98.32	90.62	0.94	93.08	100.00	82.47	0.90
	GHSL	87.92	85.52	99.60	0.92	87.94	85.95	99.58	0.92	88.56	81.03	100.00	0.90
Seoul	PLA	87.52	86.81	81.02	0.84	89.09	95.12	85.74	0.90	95.50	91.94	80.75	0.86
	RMABI	83.80	95.06	61.72	0.75	83.45	95.56	70.91	0.81	84.60	93.94	44.87	0.61
	NDMABI	86.84	94.17	71.42	0.81	87.76	95.18	80.84	0.87	86.24	91.89	53.48	0.68
	PLA + RMABI	91.29	85.77	94.09	0.90	91.71	88.89	96.97	0.93	91.10	80.23	88.06	0.84
	PLA + NDMABI	91.05	85.14	94.77	0.90	91.65	88.40	97.70	0.93	90.61	79.33	88.51	0.84
	GHSL	88.28	85.71	86.52	0.86	91.38	90.91	93.95	0.92	85.29	75.95	71.40	0.74
Delhi	PLA	90.28	94.69	85.06	0.90	67.86	100.00	57.65	0.73	95.86	89.53	63.20	0.74
	RMABI	77.48	94.79	59.16	0.73	75.93	94.98	62.99	0.76	82.47	92.59	21.11	0.34
	NDMABI	80.70	92.84	67.59	0.78	79.92	93.31	71.71	0.81	83.63	87.88	27.05	0.41
	PLA + RMABI	92.30	90.86	94.53	0.93	91.52	91.26	95.27	0.93	95.59	88.06	86.63	0.87
	PLA + NDMABI	91.98	89.76	95.38	0.92	91.07	90.00	96.15	0.93	95.53	88.06	87.11	0.88
	GHSL	82.57	81.78	86.06	0.84	80.82	80.85	89.94	0.85	87.78	92.86	47.92	0.63

(*continued on next page*)

Table A1 (*continued*)

		Overall				Urban				Rural			
		OA (%)	UA (%)	PA (%)	F	OA (%)	UA (%)	PA (%)	F	OA (%)	UA (%)	PA (%)	F
Chakwal	PLA	95.41	91.06	62.43	0.74	90.16	93.26	89.60	0.91	95.83	89.66	69.60	0.78
	RMABI	86.16	73.39	23.97	0.36	43.25	100.00	30.02	0.46	86.96	72.38	23.79	0.36
	NDMABI	86.13	73.83	23.31	0.35	42.85	100.00	29.40	0.45	86.92	72.82	23.11	0.35
	PLA + RMABI	96.03	78.54	84.12	0.81	71.83	100.00	60.78	0.76	96.37	77.58	86.21	0.82
	PLA + NDMABI	95.93	78.45	82.99	0.81	71.78	100.00	60.69	0.76	96.27	77.48	84.96	0.81
	GHSL	81.12	100.00	1.94	0.04	32.38	100.00	15.18	0.26	81.85	100.00	1.00	0.02
Riyadh	PLA	93.87	91.73	84.31	0.88	86.87	91.48	84.41	0.88	91.21	71.28	61.79	0.66
	RMABI	89.86	90.57	69.11	0.78	80.84	91.98	73.68	0.82	94.35	86.00	57.00	0.69
	NDMABI	88.74	93.51	62.06	0.75	78.94	93.96	67.81	0.79	93.41	91.67	46.90	0.62
	PLA + RMABI	92.13	78.81	96.21	0.87	86.21	82.63	97.66	0.90	95.26	69.70	92.31	0.79
	PLA + NDMABI	92.14	79.15	95.43	0.87	86.57	82.98	97.61	0.90	95.07	69.79	89.34	0.78
	GHSL	88.38	71.91	93.32	0.81	79.82	75.68	97.60	0.85	92.66	61.86	81.70	0.70
Baghdad	PLA	88.97	83.59	78.62	0.81	91.17	97.53	91.85	0.95	95.87	97.58	79.62	0.88
	RMABI	84.81	86.18	57.66	0.69	75.42	94.05	61.82	0.75	89.76	69.23	45.66	0.55
	NDMABI	88.51	84.19	75.57	0.80	86.14	93.78	81.37	0.87	89.60	64.36	60.44	0.62
	PLA + RMABI	88.42	77.02	87.76	0.82	88.76	87.60	93.62	0.91	88.00	57.14	73.91	0.64
	PLA + NDMABI	87.61	74.26	90.66	0.82	89.46	87.11	96.13	0.91	86.53	52.63	77.97	0.63
	GHSL	88.66	89.17	71.11	0.79	88.93	92.44	88.23	0.90	88.57	75.00	31.61	0.44
Addis Ababa	PLA	94.50	96.10	86.33	0.91	92.21	92.22	93.93	0.93	97.60	96.83	86.21	0.91
	RMABI	75.99	96.40	29.70	0.45	52.19	95.51	44.79	0.61	81.88	98.00	17.21	0.29
	NDMABI	77.56	95.57	34.75	0.51	59.42	97.06	52.75	0.68	82.02	92.86	19.92	0.33
	PLA + RMABI	95.35	97.31	87.42	0.92	93.61	97.60	94.74	0.96	95.91	97.01	80.70	0.88
	PLA + NDMABI	95.18	96.73	87.47	0.92	93.69	97.60	94.86	0.96	95.72	95.86	80.75	0.88
	GHSL	87.50	98.02	61.79	0.76	83.40	98.62	80.95	0.89	88.54	97.20	44.39	0.61
Nairobi	PLA	92.13	79.80	87.83	0.84	92.98	96.05	91.99	0.94	96.80	86.96	84.28	0.86
	RMABI	/	/	/	/	/	/	/	/	/	/	/	/
	NDMABI	/	/	/	/	/	/	/	/	/	/	/	/
	PLA + RMABI	/	/	/	/	/	/	/	/	/	/	/	/
	PLA + NDMABI	/	/	/	/	/	/	/	/	/	/	/	/
	GHSL	81.61	88.39	27.64	0.42	80.53	93.65	71.90	0.81	81.82	81.63	13.49	0.23
Algiers	PLA	96.90	96.01	88.09	0.92	88.20	88.28	90.84	0.90	90.17	83.78	80.59	0.82
	RMABI	82.59	98.41	27.78	0.43	69.48	100.00	42.60	0.60	85.02	97.53	22.92	0.37
	NDMABI	88.70	94.97	50.71	0.66	80.27	95.38	67.20	0.79	90.39	94.78	44.62	0.61
	PLA + RMABI	97.07	94.72	90.37	0.92	92.83	94.25	92.99	0.94	97.60	96.83	85.98	0.91
	PLA + NDMABI	96.86	93.73	90.34	0.92	92.86	92.31	95.41	0.94	97.50	94.39	88.20	0.91
	GHSL	92.81	86.57	78.11	0.82	86.41	88.37	88.54	0.88	94.09	85.79	74.32	0.80
Cape Town	PLA	95.74	91.45	89.82	0.91	94.07	95.16	96.97	0.96	98.02	78.57	65.36	0.71
	RMABI	76.81	72.73	14.69	0.24	43.06	87.50	14.22	0.24	86.33	56.76	13.94	0.22
	NDMABI	77.04	72.29	15.81	0.26	44.04	88.10	15.86	0.27	86.45	56.10	14.64	0.23
	PLA + RMABI	94.02	85.12	89.92	0.87	91.96	93.63	92.94	0.93	94.73	75.00	84.10	0.79
	PLA + NDMABI	94.05	84.88	90.32	0.88	91.96	93.63	92.99	0.93	94.80	74.63	85.02	0.79
	GHSL	89.03	70.81	97.61	0.82	80.56	77.23	100.00	0.87	91.87	63.10	93.96	0.75
Washington	PLA	89.15	86.59	89.07	0.88	92.39	96.43	91.85	0.94	95.61	84.44	80.27	0.82
	RMABI	60.94	88.14	8.80	0.16	47.19	90.00	9.63	0.17	73.25	84.21	6.34	0.12
	NDMABI	59.31	82.93	5.52	0.10	44.92	85.71	6.04	0.11	72.23	76.92	4.00	0.08
	PLA + RMABI	89.88	85.90	92.87	0.89	88.20	88.28	90.76	0.89	90.70	83.12	82.53	0.83
	PLA + NDMABI	89.38	86.29	88.55	0.87	88.20	88.28	90.84	0.90	90.52	82.58	82.54	0.83
	GHSL	78.86	70.73	88.24	0.79	75.87	71.89	95.50	0.82	82.21	68.10	72.89	0.70
Los Angeles	PLA	95.27	95.08	96.79	0.96	87.97	89.66	79.16	0.84	98.11	73.91	66.35	0.70
	RMABI	54.75	80.34	17.93	0.29	36.93	81.98	18.82	0.31	95.40	50.00	15.68	0.24
	NDMABI	55.12	80.00	18.97	0.31	37.69	82.20	20.05	0.32	95.25	42.86	14.27	0.21
	PLA + RMABI	95.92	94.96	97.23	0.96	90.64	89.54	99.57	0.94	97.79	68.42	83.81	0.75
	PLA + NDMABI	92.87	88.70	99.05	0.94	90.63	89.54	99.58	0.94	97.62	65.00	83.10	0.73
	GHSL	83.56	75.44	99.56	0.86	77.41	76.62	99.80	0.87	95.31	46.15	91.93	0.61
Santiago	PLA	94.39	92.46	89.83	0.91	89.92	95.24	75.65	0.84	97.65	95.03	83.26	0.89
	RMABI	65.79	54.69	8.45	0.15	31.77	95.83	7.26	0.14	83.89	30.00	11.27	0.16
	NDMABI	65.39	51.92	6.40	0.11	30.66	95.00	5.77	0.11	83.83	25.00	7.45	0.11
	PLA + RMABI	94.02	87.05	95.78	0.91	93.61	94.01	96.79	0.95	93.90	71.43	92.02	0.80
	PLA + NDMABI	94.15	87.27	95.71	0.91	93.88	94.36	96.82	0.96	94.07	71.43	91.69	0.80
	GHSL	89.93	95.29	74.17	0.83	83.45	95.91	80.49	0.88	93.09	92.86	56.62	0.70
Brasilia	PLA	97.51	81.58	73.30	0.77	82.02	95.63	72.87	0.83	89.38	86.67	64.58	0.74
	RMABI	94.57	79.41	20.44	0.33	76.19	100.00	36.27	0.53	96.26	65.00	14.62	0.24
	NDMABI	94.39	78.13	17.47	0.29	75.63	100.00	32.06	0.49	96.05	61.11	11.88	0.20
	PLA + RMABI	96.75	68.37	82.30	0.75	89.27	83.33	90.53	0.87	97.28	59.68	78.63	0.68
	PLA + NDMABI	96.76	68.37	82.21	0.75	89.29	83.33	90.47	0.87	97.30	59.68	78.51	0.68
	GHSL	96.21	95.35	40.49	0.57	87.72	96.00	70.75	0.81	96.97	94.44	24.41	0.39
Heidelberg	PLA	96.02	95.10	79.55	0.87	84.49	97.56	77.90	0.87	96.70	90.37	74.91	0.82
	RMABI	89.92	92.67	51.32	0.66	81.02	95.45	51.94	0.67	92.11	91.20	50.57	0.65
	NDMABI	89.91	92.67	50.96	0.66	80.98	95.45	51.60	0.67	92.11	91.20	50.19	0.65
	PLA + RMABI	97.67	91.97	93.38	0.93	95.24	92.86	92.06	0.92	98.26	91.48	93.91	0.93
	PLA + NDMABI	97.67	91.97	93.36	0.93	95.24	92.86	92.05	0.92	98.26	91.48	93.89	0.93
	GHSL	95.76	86.16	92.21	0.89	93.79	87.74	96.88	0.92	96.30	85.25	89.04	0.87

(*continued on next page*)

Table A1 (*continued*)

		Overall				Urban				Rural			
		OA (%)	UA (%)	PA (%)	F	OA (%)	UA (%)	PA (%)	F	OA (%)	UA (%)	PA (%)	F
London	PLA	94.78	91.32	97.05	0.94	87.95	92.33	88.71	0.90	93.06	87.97	78.44	0.83
	RMABI	/	/	/	/	/	/	/	/	/	/	/	/
	NDMABI	/	/	/	/	/	/	/	/	/	/	/	/
	PLA + RMABI	/	/	/	/	/	/	/	/	/	/	/	/
	PLA + NDMABI	/	/	/	/	/	/	/	/	/	/	/	/
	GHSL	90.97	85.29	95.24	0.90	87.45	86.35	97.44	0.92	93.14	82.78	90.64	0.87
Moscow	PLA	89.33	88.96	84.32	0.87	92.99	94.78	87.87	0.91	97.08	94.87	82.21	0.88
	RMABI	65.01	88.03	25.18	0.39	51.66	88.12	26.76	0.41	77.70	87.80	18.89	0.31
	NDMABI	68.81	87.69	34.42	0.49	58.32	89.51	37.33	0.53	78.43	82.69	24.28	0.38
	PLA + RMABI	89.73	86.13	91.06	0.89	89.15	89.30	93.26	0.91	90.57	79.49	84.29	0.82
	PLA + NDMABI	89.91	85.28	92.66	0.89	89.49	88.39	95.00	0.92	90.65	78.75	85.82	0.82
	GHSL	80.82	73.45	92.26	0.82	79.88	77.38	97.49	0.86	82.60	64.77	78.48	0.71
Rome	PLA	94.49	90.66	95.08	0.93	92.09	87.30	95.94	0.91	95.29	90.52	71.14	0.80
	RMABI	/	/	/	/	/	/	/	/	/	/	/	/
	NDMABI	/	/	/	/	/	/	/	/	/	/	/	/
	PLA + RMABI	/	/	/	/	/	/	/	/	/	/	/	/
	PLA + NDMABI	/	/	/	/	/	/	/	/	/	/	/	/
	GHSL	89.67	85.79	85.96	0.86	89.59	88.84	94.09	0.91	89.75	81.76	76.09	0.79
Copenhagen	PLA	96.09	90.72	85.68	0.88	86.57	83.15	96.11	0.89	92.98	77.31	82.33	0.80
	RMABI	77.89	78.57	5.68	0.11	33.60	90.91	6.94	0.13	84.55	70.59	4.96	0.09
	NDMABI	78.77	80.49	8.56	0.15	36.82	94.12	10.61	0.19	84.94	70.83	7.26	0.13
	PLA + RMABI	95.80	91.34	83.14	0.87	85.90	94.38	82.91	0.88	97.13	89.44	81.88	0.85
	PLA + NDMABI	95.79	89.54	84.88	0.87	86.93	94.44	84.63	0.89	97.05	86.58	83.92	0.85
	GHSL	91.75	87.62	67.38	0.76	77.55	86.02	80.31	0.83	93.66	88.99	56.24	0.69
Paris	PLA	91.19	91.50	88.02	0.90	93.45	93.64	97.33	0.95	95.60	86.93	96.40	0.91
	RMABI	81.48	92.42	61.77	0.74	76.45	94.63	68.22	0.79	85.75	86.36	48.04	0.62
	NDMABI	87.74	91.24	77.60	0.84	86.33	93.92	84.04	0.89	88.82	84.35	62.87	0.72
	PLA + RMABI	93.07	90.04	93.56	0.92	92.94	92.54	96.96	0.95	93.26	84.35	85.65	0.85
	PLA + NDMABI	92.83	88.84	94.76	0.92	92.37	91.23	97.77	0.94	93.24	83.44	87.84	0.86
	GHSL	89.85	82.87	96.54	0.89	86.50	83.20	100.00	0.91	92.54	82.05	88.92	0.85
Sydney	PLA	92.30	95.23	89.80	0.92	94.35	93.18	96.98	0.95	94.89	87.70	91.14	0.89
	RMABI	/	/	/	/	/	/	/	/	/	/	/	/
	NDMABI	/	/	/	/	/	/	/	/	/	/	/	/
	PLA + RMABI	/	/	/	/	/	/	/	/	/	/	/	/
	PLA + NDMABI	/	/	/	/	/	/	/	/	/	/	/	/
	GHSL	92.24	88.84	98.02	0.93	92.18	90.51	98.59	0.94	92.46	81.82	95.45	0.88
Perth	PLA	95.78	94.40	84.65	0.89	91.66	97.05	89.03	0.93	93.10	89.22	84.77	0.87
	RMABI	79.33	76.25	22.11	0.34	65.81	80.85	27.91	0.41	84.33	69.70	16.78	0.27
	NDMABI	81.43	75.83	31.72	0.45	70.77	81.16	40.61	0.54	85.33	68.63	23.49	0.35
	PLA + RMABI	95.26	90.95	85.63	0.88	90.97	90.08	87.72	0.89	96.83	91.80	83.38	0.87
	PLA + NDMABI	95.15	86.30	92.20	0.89	91.66	88.37	93.34	0.91	96.56	84.40	91.28	0.88
	GHSL	88.00	71.43	86.35	0.78	82.13	73.42	95.44	0.83	90.16	69.23	77.58	0.73

PLA: the results generated by using the planar features (i.e., MBI and Harris corner).
RMABI: the results generated by using RMABI feature individually.
NDMABI: the results generated by using single NDMABI feature individually.
PLA + RMABI: the results generated by the fusion of the planar features and RMABI.
PLA + NDMABI: the results generated by the fusion of the planar features and NDMABI.

References

Aguilar, M.A., del Mar Saldaña, M., Aguilar, F.J., 2014. Generation and quality assessment of stereo-extracted DSM from GeoEye-1 and WorldView-2 imagery. IEEE Trans. Geosci. Remote Sens. 52, 1259–1271.

Arino, O., Gross, D., Ranera, F., Leroy, M., Bicheron, P., Brockman, C., Defourny, P., Vancutsem, C., Achard, F., Durieux, L., 2007. GlobCover: ESA service for global land cover from MERIS. In: Geoscience and Remote Sensing Symposium, 2007. IGARSS 2007. IEEE International. IEEE, pp. 2412–2415.

Bhaduri, B., Bright, E., Coleman, P., Dobson, J., 2002. LandScan. Geoinformatics 5, 34–37.

Bontemps, S., Defourny, P., Bogaert, E.V., Arino, O., Kalogirou, V., Perez, J.R., 2011. GLOBCOVER 2009-products description and validation report. In: ESA Technical Report.

Brockmann, D., Helbing, D., 2013. The hidden geometry of complex, network-driven contagion phenomena. science 342, 1337–1342.

Chavez, P., Sides, S.C., Anderson, J.A., 1991. Comparison of three different methods to merge multiresolution and multispectral data- Landsat TM and SPOT panchromatic. Photogramm. Eng. Remote. Sens. 57, 295–303.

Chen, J., Chen, J., Liao, A., Cao, X., Chen, L., Chen, X., He, C., Han, G., Peng, S., Lu, M., 2015. Global land cover mapping at 30 m resolution: a POK-based operational approach. ISPRS J. Photogramm. Remote Sens. 103, 7–27.

Dare, P.M., 2005. Shadow analysis in high-resolution satellite imagery of urban areas. Photogramm. Eng. Remote Sens. 71, 169–177.

Deng, C., Wu, C., 2012. BCI: a biophysical composition index for remote sensing of urban environments. Remote Sens. Environ. 127, 247–259.

Elvidge, C.D., Imhoff, M.L., Baugh, K.E., Hobson, V.R., Nelson, I., Safran, J., Dietz, J.B., Tuttle, B.T., 2001. Night-time lights of the world: 1994–1995. ISPRS J. Photogramm. Remote Sens. 56, 81–99.

Elvidge, C.D., Tuttle, B.T., Sutton, P.C., Baugh, K.E., Howard, A.T., Milesi, C., Bhaduri, B., Nemani, R., 2007. Global distribution and density of constructed impervious surfaces. Sensors 7, 1962–1979.

Esch, T., Taubenböck, H., Roth, A., Heldens, W., Felbier, A., Schmidt, M., Mueller, A.A., Thiel, M., Dech, S.W., 2012. TanDEM-X mission-new perspectives for the inventory and monitoring of global settlement patterns. J. Appl. Remote. Sens. 6, 061702.

Esch, T., Marconcini, M., Felbier, A., Roth, A., Heldens, W., Huber, M., Schwinger, M., Taubenböck, H., Müller, A., Dech, S., 2013. Urban footprint processor—fully automated processing chain generating settlement masks from global data of the TanDEM-X mission. IEEE Geosci. Remote Sens. Lett. 10, 1617–1621.

Esch, T., Heldens, W., Hirner, A., Keil, M., Marconcini, M., Roth, A., Zeidler, J., Dech, S., Strano, E., 2017. Breaking new ground in mapping human settlements from space–the global urban footprint. ISPRS J. Photogramm. Remote Sens. 134, 30–42.

Florczyk, A.J., Ferri, S., Syrris, V., Kemper, T., Halkia, M., Soille, P., Pesaresi, M., 2016. A new European settlement map from optical remotely sensed data. IEEE J. Select. Top. Appl. Earth Observ. Rem. Sens. 9, 1978–1992.

Foley, J.A., Ramankutty, N., Brauman, K.A., Cassidy, E.S., Gerber, J.S., Johnston, M., Mueller, N.D., O'Connell, C., Ray, D.K., West, P.C., 2011. Solutions for a cultivated

planet. Nature 478, 337.
Foody, G.M., 2002. Status of land cover classification accuracy assessment. Remote Sens. Environ. 80, 185–201.
Gamba, P., Herold, M., 2009. Global Mapping of Human Settlement: Experiences, Datasets, and Prospects. CRC Press.
Gong, P., Liang, S., Carlton, E.J., Jiang, Q., Wu, J., Wang, L., Remais, J.V., 2012. Urbanisation and health in China. Lancet 379, 843–852.
Gong, P., Wang, J., Yu, L., Zhao, Y., Zhao, Y., Liang, L., Niu, Z., Huang, X., Fu, H., Liu, S., 2013. Finer resolution observation and monitoring of global land cover: first mapping results with Landsat TM and ETM+ data. Int. J. Remote Sens. 34, 2607–2654.
Grekousis, G., Mountrakis, G., Kavouras, M., 2015. An overview of 21 global and 43 regional land-cover mapping products. Int. J. Remote Sens. 36, 5309–5335.
Gueguen, L., Pesaresi, M., 2011. Multi scale Harris corner detector based on differential morphological decomposition. Pattern Recogn. Lett. 32, 1714–1719.
Harris, C., Stephens, M., 1988. A combined corner and edge detector. In: Alvey Vision Conference. Citeseer, pp. 10.5244.
Hirschmuller, H., 2008. Stereo processing by semiglobal matching and mutual information. In: IEEE Transactions on pattern analysis and machine intelligence. 30. pp. 328–341.
Hu, T., Huang, X., Li, J., Zhang, L., 2018. A novel co-training approach for urban land cover mapping with unclear Landsat time series imagery. Remote Sens. Environ. 217, 144–157.
Hu, Z., Li, Q., Zhang, Q., Wu, G., 2016. Representation of block-based image features in a multi-scale framework for built-up area detection. Remote Sens. 8, 155.
Huang, X., Zhang, L., 2011. A multidirectional and multiscale morphological index for automatic building extraction from multispectral GeoEye-1 imagery. Photogramm. Eng. Remote Sens. 77, 721–732.
Huang, X., Zhang, L., 2012. Morphological building/shadow index for building extraction from high-resolution imagery over urban areas. IEEE J. Select. Top. Appl. Earth Observ. Rem. Sens. 5, 161–172.
Huang, X., Wen, D., Li, J., Qin, R., 2017a. Multi-level monitoring of subtle urban changes for the megacities of China using high-resolution multi-view satellite imagery. Remote Sens. Environ. 196, 56–75.
Huang, X., Yuan, W., Li, J., Zhang, L., 2017b. A new building extraction postprocessing framework for high-spatial-resolution remote-sensing imagery. IEEE J. Select. Top. Appl. Earth Observ. Rem. Sens. 10, 654–668.
Huang, X., Chen, H., Gong, J., 2018a. Angular difference feature extraction for urban scene classification using ZY-3 multi-angle high-resolution satellite imagery. ISPRS J. Photogramm. Remote Sens. 135, 127–141.
Huang, X., Hu, T., Li, J., Wang, Q., Benediktsson, J.A., 2018b. Mapping urban areas in China using multisource data with a novel ensemble SVM method. IEEE Trans. Geosci. Remote Sens. 1–16.
Huete, A.R., 1988. A soil-adjusted vegetation index (SAVI). Remote Sens. Environ. 25, 295–309.
Klotz, M., Kemper, T., Geiß, C., Esch, T., Taubenböck, H., 2016. How good is the map? A multi-scale cross-comparison framework for global settlement layers: evidence from Central Europe. Remote Sens. Environ. 178, 191–212.
Kovács, A., Szirányi, T., 2013. Improved Harris feature point set for orientation-sensitive urban-area detection in aerial images. IEEE Geosci. Remote Sens. Lett. 10, 796–800.
Leyk, S., Uhl, J.H., Balk, D., Jones, B., 2018. Assessing the accuracy of multi-temporal built-up land layers across rural-urban trajectories in the United States. Remote Sens. Environ. 204, 898–917.
Li, X., Gong, P., Liang, L., 2015a. A 30-year (1984–2013) record of annual urban dynamics of Beijing City derived from Landsat data. Remote Sens. Environ. 166, 78–90.
Li, Y., Tan, Y., Li, Y., Qi, S., Tian, J., 2015b. Built-up area detection from satellite images using multikernel learning, multifield integrating, and multihypothesis voting. IEEE Geosci. Remote Sens. Lett. 12, 1190–1194.
Longbotham, N., Chaapel, C., Bleiler, L., Padwick, C., Emery, W.J., Pacifici, F., 2012. Very high resolution multiangle urban classification analysis. IEEE Trans. Geosci. Remote Sens. 50, 1155–1170.
Matasci, G., Longbotham, N., Pacifici, F., Kanevski, M., Tuia, D., 2015. Understanding angular effects in VHR imagery and their significance for urban land-cover model portability: a study of two multi-angle in-track image sequences. ISPRS J. Photogramm. Remote Sens. 107, 99–111.
McFeeters, S.K., 1996. The use of the normalized difference water index (NDWI) in the delineation of open water features. Int. J. Remote Sens. 17, 1425–1432.
Melchiorri, M., Florczyk, A.J., Freire, S., Schiavina, M., Pesaresi, M., Kemper, T., 2018. Unveiling 25 years of planetary urbanization with remote sensing: perspectives from the global human settlement layer. Remote Sens. 10, 768.
Ngo, T.-T., Mazet, V., Collet, C., de Fraipont, P., 2017. Shape-based building detection in visible band images using shadow information. IEEE J. Select. Top. Appl. Earth Observ. Rem. Sens. 10, 920–932.
Ok, A.O., 2013. Automated detection of buildings from single VHR multispectral images using shadow information and graph cuts. ISPRS J. Photogramm. Remote Sens. 86, 21–40.
Olofsson, P., Foody, G.M., Herold, M., Stehman, S.V., Woodcock, C.E., Wulder, M.A., 2014. Good practices for estimating area and assessing accuracy of land change. Remote Sens. Environ. 148, 42–57.
Pelizari, P.A., Spröhnle, K., Geiß, C., Schoepfer, E., Plank, S., Taubenböck, H., 2018. Multi-sensor feature fusion for very high spatial resolution built-up area extraction in temporary settlements. Remote Sens. Environ. 209, 793–807.
Pesaresi, M., Benediktsson, J.A., 2001. A new approach for the morphological segmentation of high-resolution satellite imagery. IEEE Trans. Geosci. Remote Sens. 39, 309–320.
Pesaresi, M., Gerhardinger, A., Kayitakire, F., 2008. A robust built-up area presence index by anisotropic rotation-invariant textural measure. IEEE J. Select. Top. Appl. Earth Observ. Rem. Sens. 1, 180–192.
Pesaresi, M., Ehrlich, D., Caravaggi, I., Kauffmann, M., Louvrier, C., 2011. Toward global automatic built-up area recognition using optical VHR imagery. IEEE J. Select. Top. Appl. Earth Observ. Rem. Sens. 4, 923–934.
Pesaresi, M., Guo, H.D., Blaes, X., Ehrlich, D., Ferri, S., Gueguen, L., Halkia, M., Kauffmann, M., Kemper, T., Lu, L.L., Marin-Herrera, M.A., Ouzounis, G.K., Scavazzon, M., Soille, P., Syrris, V., Zanchetta, L., 2013. A global human settlement layer from optical HR/VHR RS data: concept and first results. IEEE J. Select. Top. Appl. Earth Observ. Rem. Sens. 6, 2102–2131.
Pesaresi, M., Ehrilch, D., Florczyk, A., Freire, S., Julea, A., Kemper, T., Soille, P., Syrris, V., 2015. GHS Built-Up Grid, Derived from Landsat, Multitemporal (1975, 1990, 2000, 2014). European Commission, Joint Research Centre (JRC).
Pesaresi, M., Ehrlich, D., Ferri, S., Florczyk, A., Freire, S., Halkia, M., Julea, A., Kemper, T., Soille, P., Syrris, V., 2016. Operating Procedure for the Production of the Global Human Settlement Layer from Landsat Data of the Epochs 1975, 1990, 2000, and 2014. Publications Office of the European Union, Luxembourg.
Potere, D., Schneider, A., Angel, S., Civco, D.L., 2009. Mapping urban areas on a global scale: which of the eight maps now available is more accurate? Int. J. Remote Sens. 30, 6531–6558.
Qin, R., Fang, W., 2014. A hierarchical building detection method for very high resolution remotely sensed images combined with DSM using graph cut optimization. Photogramm. Eng. Remote Sens. 80, 873–883.
Qin, Y., Xiao, X., Dong, J., Chen, B., Liu, F., Zhang, G., Zhang, Y., Wang, J., Wu, X., 2017. Quantifying annual changes in built-up area in complex urban-rural landscapes from analyses of PALSAR and Landsat images. ISPRS J. Photogramm. Remote Sens. 124, 89–105.
Schneider, A., 2012. Monitoring land cover change in urban and peri-urban areas using dense time stacks of Landsat satellite data and a data mining approach. Remote Sens. Environ. 124, 689–704.
Schneider, A., Mertes, C., 2014. Expansion and growth in Chinese cities, 1978–2010. Environ. Res. Lett. 9, 024008.
Schneider, A., Woodcock, C.E., 2008. Compact, dispersed, fragmented, extensive? A comparison of urban growth in twenty-five global cities using remotely sensed data, pattern metrics and census information. Urban Stud. 45, 659–692.
Schneider, A., Friedl, M.A., Potere, D., 2009. A new map of global urban extent from MODIS satellite data. Environ. Res. Lett. 4, 044003.
Schneider, A., Friedl, M.A., Potere, D., 2010. Mapping global urban areas using MODIS 500-m data: new methods and datasets based on 'urban ecoregions'. Remote Sens. Environ. 114, 1733–1746.
Sexton, J.O., Song, X.-P., Huang, C., Channan, S., Baker, M.E., Townshend, J.R., 2013. Urban growth of the Washington, DC–Baltimore, MD metropolitan region from 1984 to 2010 by annual, Landsat-based estimates of impervious cover. Remote Sens. Environ. 129, 42–53.
Sirmacek, B., Unsalan, C., 2010. Urban area detection using local feature points and spatial voting. IEEE Geosci. Remote Sens. Lett. 7, 146–150.
Song, H., Huang, B., Zhang, K., 2014. Shadow detection and reconstruction in high-resolution satellite images via morphological filtering and example-based learning. IEEE Trans. Geosci. Remote Sens. 52, 2545–2554.
Song, X.-P., Sexton, J.O., Huang, C., Channan, S., Townshend, J.R., 2016. Characterizing the magnitude, timing and duration of urban growth from time series of Landsat-based estimates of impervious cover. Remote Sens. Environ. 175, 1–13.
Stehman, S.V., 2013. Estimating area from an accuracy assessment error matrix. Remote Sens. Environ. 132, 202–211.
Sun, G., Chen, X., Jia, X., Yao, Y., Wang, Z., 2016. Combinational build-up index (CBI) for effective impervious surface mapping in urban areas. IEEE J. Select. Top. Appl. Earth Observ. Rem. Sens. 9, 2081–2092.
Tang, X., Zhang, G., Zhu, X., Pan, H., Jiang, Y., Zhou, P., Wang, X., 2013. Triple linear-array image geometry model of ZiYuan-3 surveying satellite and its validation. Int. J. Image Data Fus. 4, 33–51.
Tang, X., Zhou, P., Zhang, G., Wang, X., Jiang, Y., Guo, L., Liu, S., 2015. Verification of ZY-3 satellite imagery geometric accuracy without ground control points. IEEE Geosci. Remote Sens. Lett. 12, 2100–2104.
Tao, C., Tan, Y., Zou, Z.-r., Tian, J., 2013. Unsupervised detection of built-up areas from multiple high-resolution remote sensing images. IEEE Geosci. Remote Sens. Lett. 10, 1300–1304.
Tatem, A.J., Noor, A.M., Hay, S.I., 2005. Assessing the accuracy of satellite derived global and national urban maps in Kenya. Remote Sens. Environ. 96, 87–97.
Taubenböck, H., Klotz, M., Wurm, M., Schmieder, J., Wagner, B., Wooster, M., Esch, T., Dech, S., 2013. Delineation of central business districts in mega city regions using remotely sensed data. Remote Sens. Environ. 136, 386–401.
Tong, X., Li, L., Liu, S., Xu, Y., Ye, Z., Jin, Y., Wang, F., Xie, H., 2015. Detection and estimation of ZY-3 three-line array image distortions caused by attitude oscillation. ISPRS J. Photogramm. Remote Sens. 101, 291–309.
United Nations, 2017. World Population Prospects: The 2017 Revision. Population Division, Department of Economic and Social Affairs: United Nations Publications.
United Nations, 2018. World Urbanization Prospects: The 2018 Revision. Population Division, Department of Economic and Social Affairs: United Nations Publications.
Wang, T., Zhang, G., Li, D., Tang, X., Jiang, Y., Pan, H., Zhu, X., Fang, C., 2014. Geometric accuracy validation for ZY-3 satellite imagery. IEEE Geosci. Remote Sens. Lett. 11, 1168–1171.
Xin, X., Liu, B., Di, K., Zhu, Z., Zhao, Z., Liu, J., Yue, Z., Zhang, G., 2017. Monitoring urban expansion using time series of night-time light data: a case study in Wuhan, China. Int. J. Remote Sens. 38, 6110–6128.
Yang, X., Yue, W., Gao, D., 2013. Spatial improvement of human population distribution based on multi-sensor remote-sensing data: an input for exposure assessment. Int. J. Remote Sens. 34, 5569–5583.

Yuan, F., Sawaya, K.E., Loeffelholz, B.C., Bauer, M.E., 2005. Land cover classification and change analysis of the twin cities (Minnesota) metropolitan area by multitemporal Landsat remote sensing. Remote Sens. Environ. 98, 317–328.
Zhang, L., Weng, Q., 2016. Annual dynamics of impervious surface in the Pearl River Delta, China, from 1988 to 2013, using time series Landsat imagery. ISPRS J. Photogramm. Remote Sens. 113, 86–96.
Zhang, Q., Seto, K.C., 2011. Mapping urbanization dynamics at regional and global scales using multi-temporal DMSP/OLS nighttime light data. Remote Sens. Environ. 115, 2320–2329.
Zhou, Y., Smith, S.J., Elvidge, C.D., Zhao, K., Thomson, A., Imhoff, M., 2014. A cluster-based method to map urban area from DMSP/OLS nightlights. Remote Sens. Environ. 147, 173–185.
Zhou, Y., Smith, S.J., Zhao, K., Imhoff, M., Thomson, A., Bond-Lamberty, B., Asrar, G.R., Zhang, X., He, C., Elvidge, C.D., 2015. A global map of urban extent from nightlights. Environ. Res. Lett. 10, 054011.
Zhu, Z., Woodcock, C.E., Rogan, J., Kellndorfer, J., 2012. Assessment of spectral, polarimetric, temporal, and spatial dimensions for urban and peri-urban land cover classification using Landsat and SAR data. Remote Sens. Environ. 117, 72–82.